ELSEVIER

Journal of Nuclear Materials 300 (2002) 91–117

journal of nuclear materials

www.elsevier.com/locate/jnucmat

Review

Hydrogen isotope retention and recycling in fusion reactor plasma-facing components

Rion A. Causey *

Sandia National Laboratories, MS 9402, P.O. Box 969, Livermore, CA 94550, USA

Received 4 May 2001; accepted 9 October 2001

Abstract

The proper design of a fusion reactor is not possible unless there is an understanding of the hydrogen isotope retention and recycling for the plasma-facing components. From the tritium inventory point of view, it is absolutely necessary to understand the short-term and long-term hydrogen isotopes retention characteristics of the individual materials used for the first wall and divertor. From the plasma density and fueling point of view, it is necessary to understand the recycling characteristics of these materials. This report is an overview of the available data on hydrogen isotope retention and recycling for beryllium, tungsten, carbon, and selected liquid metals. For each material discussed, recommendations are made as to the most appropriate values to use for parameters such as diffusivity, solubility, recombination rate coefficient, and trapping.

PACS: 01.30.R; 28.52; 66.30

1. Introduction

The design of a fusion reactor requires an understanding of the hydrogen isotope (protium, deuterium, and tritium) retention and recycling that will occur during operation. Retention of the hydrogen isotopes is particularly important if the isotope is tritium. Retention of large quantities of tritium in the reactor plasma-facing components increases the fuel costs of the reactor and presents a safety concern. Recycling is the rate of return of the cold hydrogen to the plasma, controlling the fueling rate and lowering the plasma temperature. The topic of hydrogen isotope retention and recycling in plasma-facing materials has been reviewed previously [1–8].

The different processes controlling the retention as well as the recycling of the hydrogen isotopes in the plasma-facing components are shown in Fig. 1. A fraction of the ions striking the surface are directly scattered back into the plasma. The number of particles promptly returned to the plasma by this scattering process depends on the incident energy of the incoming particles as well as the type of material. Because these particles do not come to rest within the plasma-facing material, this process will not be covered in this review. Particles stopping in the material have several possible fates. Previously existing defects, defects resulting from fusion neutrons, and defects caused by the energetic hydrogen ions may trap hydrogen atoms in the implantation zone, defined by the maximum range of the incident hydrogen. In the extreme case where the hydrogen solubility is very low in the implanted material, molecular recombination within the implantation zone may occur. Bubble coalescence can eventually lead to an open porous implant layer. In the more normal case, the traps eventually become saturated, and the untrapped hydrogen atoms diffuse out of the implant zone, going either deeper into the material or to the front surface. Those atoms heading deeper into the material will eventually find traps outside of the implant zone, or will reach the backside of the material.

* Tel.: +1-925 294 3326; fax: +1-925 294 3231.
E-mail address: causey@ca.sandia.gov (R.A. Causey).

0022-3115/02/$ - see front matter
PII: S0022-3115(01)00732-2

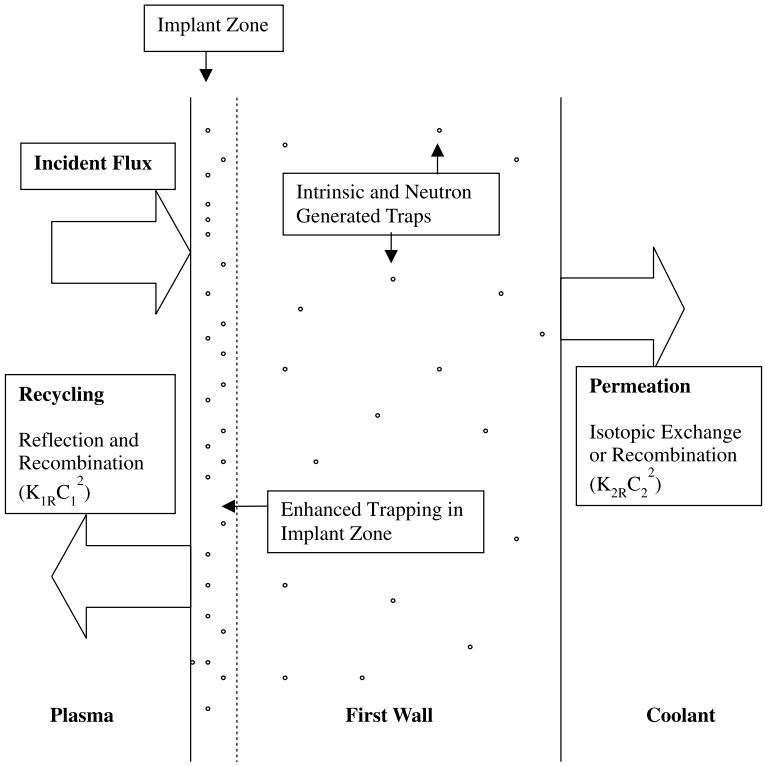

Fig. 1. Processes involved in the hydrogen isotope retention and recycling in fusion reactor plasma-facing materials.

Hydrogen atoms reaching either surface are not guaranteed immediate release. At the plasma-facing surface, with the exception of extremely high temperatures, recombination of the atoms into molecules must occur before release is possible. A high recombination rate coefficient leads to rapid release of atoms reaching the surface, effectively driving the hydrogen isotope concentration at the surface towards zero. A low recombination coefficient leads to a low release rate at the front surface, forcing many of the implanted atoms to diffuse into the material away from the implanted surface. The low recombination rate coefficient leads to higher inventories of the hydrogen isotopes in the material with potentially higher release rates out of the rear of the plasma-facing material (permeation). If the coolant is water, isotopic exchange with the protium in the water is the typical means of release from that surface. If the coolant is helium, molecular recombination will be required for release to occur. A lithium coolant would likely promote rapid release with the hydrogen atoms reacting with the liquid metal. When the hydrogen isotope is tritium, permeation leads to contamination of the liquid or gas coolant at the rear of the plasma-facing surface.

This overview of the hydrogen isotope retention and recycling in plasma-facing materials is divided into sections. Each section reviews the different material parameters such as diffusivity, solubility, trapping, and recombination rate coefficient. The first section is on beryllium with a review of hydrogen migration parameters, implantation and surface effects, tokamak results, codeposition properties, and finally, a section on internal breeding of tritium. The second section is on tungsten with a review of hydrogen migration parameters, implantation and surface effects, and codeposition properties. The third section reviews carbon. Because carbon has such unique behavior in tokamak operation, the format for this section is different. This section is broken down into segments on the saturated layer, the codeposited layer, absorption on internal porosity, intergranular migration, and dopants. The final section of the review is hydrogen isotope retention and recycling in liquid metals. These materials are now receiving consideration for use in magnetic fusion devices as well as inertial confinement fusion reactors.

2. Background

Diffusivity, solubility, trapping, and recombination are discussed throughout each section of this paper. Background information on these processes is presented in this section.

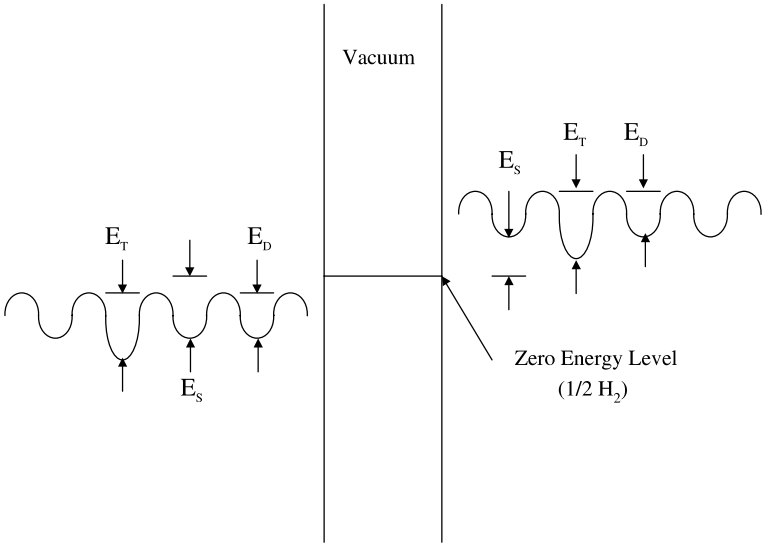

Fig. 2. Potential energy diagram for hydrogen in materials.

Fig. 2 shows the potential energy diagram for hydrogen in materials. Two different cases are shown, that for an endothermic material and that for an exothermic material. An endothermic material is one in which energy must be added to introduce hydrogen into solution. The solubility, or amount of absorbed hydrogen for a particular exposure pressure, increases with temperature for the endothermic materials. Exothermic materials are ones in which there is a chemical affinity for the hydrogen. The hydrogen solubilities in these materials decrease with increasing temperature. Examples of these exothermic materials are vanadium, palladium, and zirconium. In the figure shown, the zero energy point is defined as that of one-half the energy of the H_2 molecule. The expression for the concentration of hydrogen at the surface of a material (or the equilibrium concentration throughout the material after long-term exposure) exposed to hydrogen gas at a pressure p is

$$C = Sp^{1/2} \quad \text{where}$$
$$S = S_0 \exp(-E_S/kT) \quad ((\mathrm{H/M})\ \mathrm{atm}^{-1/2})$$

In this expression, E_S is the solubility activation energy, T is the absolute temperature, and H/M is the ratio of hydrogen atoms to metal atoms. E_S can be seen in the figure as the difference between the energy of the atom in solution and that of the zero energy point. For fusion applications where the hydrogen is driven directly into the material without going through the absorption process, it is not apparent that solubility is important. However, solubility not only plays an important role in determining the recombination rate coefficient (see below), but also determines whether bubbles and blisters are likely to occur during implantation. A material with a very low hydrogen solubility is likely to have hydrogen come out of solution at defects such as vacancies, voids, and cell boundaries, forming bubbles and blisters.

The rate at which hydrogen moves through a material is defined by the expression

$$D = D_0 \exp(-E_D/kT) \quad (\mathrm{m}^2/\mathrm{s}).$$

Here E_D is the activation energy for diffusion and T is the absolute temperature. It can be seen in Fig. 2 that E_D is the energy barrier that must be overcome for an atom to move from one equilibrium site in the lattice to another. The leading coefficient, D_0, can be thought of as the product of the jump frequency times the effective jump distance. The exponential can be thought of as the probability of the hydrogen atom actually making a successful jump through the barrier to the next site.

Throughout this paper, trap energies for hydrogen isotopes in the different materials are discussed. Defects such as vacancies, voids, and cell boundaries are sites where hydrogen achieves a potential energy below that of the normal solution site. For the hydrogen atom to escape from such a trap, it must overcome not only the energy difference between the trap site and that of the normal solution site, but must also pass through the diffusion barrier, E_D, as well. This total energy is defined as the trap energy, E_T. It is demonstrated in Fig. 2 as well. For a more complete description of hydrogen diffusion, solubility, and trapping, the reader should consult Refs. [9–11].

When high concentrations of hydrogen are generated in the very near surface of a material by implantation in

a tokamak, the material tries to come into equilibrium with the low neutral gas pressure in the fusion chamber by rapidly releasing the hydrogen molecules. The hydrogen isotope recombination process is defined by the expression

$$\text{Release rate} = K_R C^2 \quad (\text{atoms/m}^2\,\text{s}).$$

Here, K_R is the recombination rate coefficient and C is the hydrogen isotope concentration immediately below the surface. A material with a high recombination rate coefficient promotes rapid release from the surface, keeping the overall hydrogen isotope concentration low throughout the material. A material with a low recombination rate coefficient prevents rapid release, elevating the hydrogen isotope concentration throughout the material and increasing the release rate out of the rear of the material.

The reader is referred to reports by Pick and Sonnenberg [12], Baskes [13], and Wampler [14] for derivations and discussion of the recombination rate coefficient. All of the above reports have the common trait of having the recombination rate coefficient inversely proportional to the square of the solubility. All of the models also account for the fact that surface impurities can impede the recombination rate. The Baskes [13] model differs from the other two models in assuming that the recombination rate can be controlled by the arrival rate of atoms at the surface when the implantation rate is extremely high (a majority of the available surface sites are filled). This assumption results in his expression for the coefficient including the diffusive term $\exp(-2E_D/kT)$ for endothermic materials.

3. Beryllium

For present-day fusion devices, beryllium is one of the candidates for use on the first wall. Its usefulness is based on its low atomic number, its ability to remove oxygen from the plasma through chemical gettering, and its ability to pump hydrogen almost continuously during short discharges. This hydrogen pumping occurs even though it appears that the equilibrium solubility of hydrogen isotopes in beryllium is extremely low (or even zero).

3.1. Diffusivity

Fig. 3 shows the Arrhenius plot (exponential temperature dependence) for diffusivities of hydrogen isotopes in beryllium as determined by various research groups [15–17]. Jones and Gibson [15] studied both tritium diffusion and solubility in arc-cast beryllium at temperatures from 673 to 1173 K. In their experiments, beryllium was exposed to tritium gas for various times,

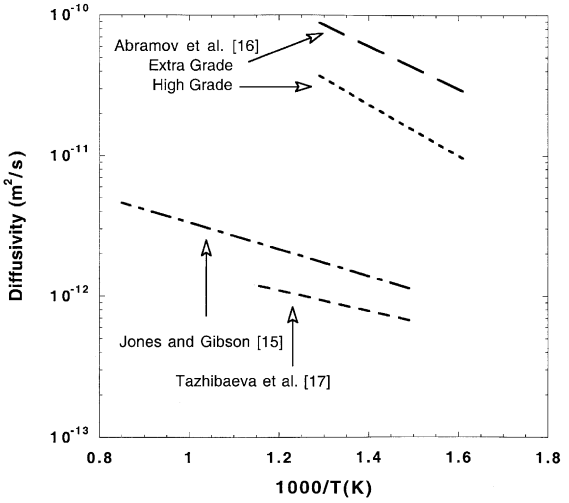

Fig. 3. Hydrogen diffusivity in beryllium.

temperatures, and pressures during isothermal anneals. Samples were then moved to another part of the apparatus and heated to selected temperatures. Small amounts of hydrogen gas were present in the apparatus to dilute the released tritium. In all cases, the release was not typical of normal diffusion. At a given temperature, the release would eventually drop to almost zero, only to rise again after the temperature was increased. It was possible to repeat this stepwise increase in release several times for each sample. Relatively thick oxide layers are likely to have affected the results. Still, the data were analyzed by fitting the logarithm of fractional release versus time to determine the diffusivity at each of the anneal temperatures. Their expression for the diffusivity is given by: $D = 3 \times 10^{-11} \exp(-0.19\ \text{eV}/kT)\ \text{m}^2/\text{s}$.

Abramov et al. [16] determined the diffusivity of deuterium in beryllium using the gas-driven permeation technique. Two different high purity (99% and 99.8%) beryllium materials were used in the experiments. Multilayer permeation theory was used in the data analysis to take into consideration the effect of the oxide layer on the permeation. For the high grade (99%) beryllium, the Arrhenius equation for the diffusivity is: $D = 8.0 \times 10^{-9} \exp(-0.36\ \text{eV}/kT)\ \text{m}^2/\text{s}$. For the extra-grade beryllium, the diffusivity is given by: $D = 6.7 \times 10^{-9} \exp(-0.29\ \text{eV}/kT)\ \text{m}^2/\text{s}$. In a similar study, Tazhibaeva et al. [17] determined diffusivities for deuterium in 98% pure beryllium using the gas-driven permeation technique. Like the Abramov et al. [16] work, they used the multilayer analysis technique to account for the effect of the oxide layer. Over the temperature range of 673–873 K, they reported the diffusivity to be: $D = 9 \times 10^{-12} \exp(-0.15\ \text{eV}/kT)\ \text{m}^2/\text{s}$.

In a series of experiments, Thomson and Macauley-Newcombe [18,19] examined the diffusion of deuterium

in single crystal and polycrystalline beryllium. For experiments where the deuterium was loaded from the gas phase at elevated temperatures, the effective diffusivity of the deuterium in the single crystal material was lower than that for polycrystalline material. They reported that the diffusivity given by Abramov et al. [16] gave a good fit to the data for the polycrystalline beryllium. When the authors attempted to make similar measurements using implanted deuterium, they found that the effective diffusivity in the single crystals was enhanced by the beam. They suggested that the diffusivity measured for deuterium in single crystals during gas loading was the 'real' diffusivity for deuterium in beryllium, and that other measurements were affected by 'short circuit' diffusion along grain boundaries.

3.2. Solubility

Fig. 4 shows the Arrhenius plot for solubilities of hydrogen isotopes in beryllium as given by various research groups [15,20,21]. Jones and Gibson [15] determined the solubility of tritium in arc-cast beryllium by exposing samples to gas at fixed pressures and temperatures for times varying from 15 to 144 h. They determined the solubility to be effectively independent of temperature. From approximately 550 to 1250 K, the solubility of tritium in beryllium was reported to be a constant 6.4 appm T/Be $\text{atm}^{1/2}$.

Swansiger [20] used 98.5% and 99.8% pure beryllium in experiments on tritium solubility in beryllium using the gas uptake technique. He noted no strong effects of either sample thickness or sample purity on solubility. From 713 to 783 K the solubility was reported to be: $S = 18.2\exp(-1.0\ \text{eV}/kT)$ T/Be $\text{atm}^{1/2}$. While the amount of absorbed tritium decreased rapidly with decreasing temperature for temperatures from 783 to 713 K, it rose again as the temperature was dropped below 650 K. This effect was suggested to be due to trapping. Shapovalov and Dukel'skii [21] used hydrogenation to equilibrium at various hydrogen pressures with quenching and vacuum extraction to determine the solubility of hydrogen in sintered, distilled alpha beryllium. For the temperature range 673–1473 K, they reported the solubility to be given by: $S = 5.8 \times 10^{-5}\exp(-0.174\ \text{eV}/kT)$ H/Be $\text{atm}^{1/2}$. It is interesting to look back at Fig. 4 and compare the three different reported solubilities. Over the temperature ranges where the measurements were performed, all of the reported solubilities agree within an order of magnitude or less even though the reported activation energies vary by as much as 1 eV!

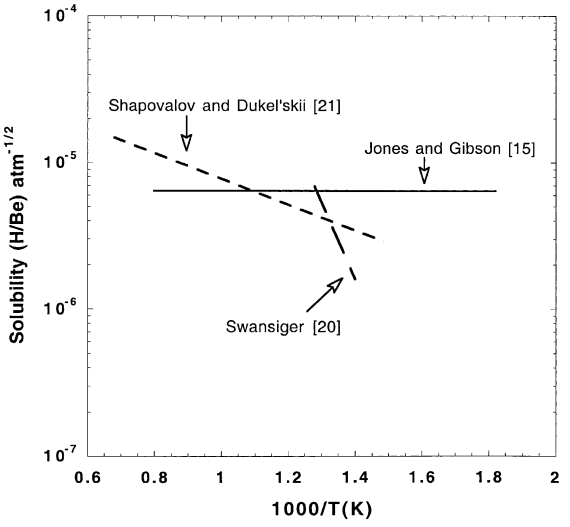

Fig. 4. Hydrogen solubility in beryllium.

3.3. Permeation

The gas phase permeation of hydrogen through 98.4% purity powder metallurgy beryllium was measured by Al'tovshiy et al. [22] using both tubes and membranes. Pressures were varied from 3 to 21 atm while temperatures varied from 773 up to 923 K. Because no attempt was made to consider the effects of the oxide layer, it is not surprising that the data varied considerably depending on the type of experiment performed. For the tubes, the activation energy of the permeation was determined to be 0.91 eV while that for the membranes was 0.28 eV. The authors did report that the permeation was affected by the grain size of the material with permeation decreasing as the grain size decreased.

Abramov et al. [16] also used the gas-driven technique to examine hydrogen isotope permeation through beryllium, but they were very careful in their consideration of the surface oxide. While selected values for the permeation were shown in their discussion of the pressure dependence of permeation (ex. $P = 2.1 \times 10^{17}$ D/$\text{m}^2\,\text{s}$ at 725 K and a pressure of 5×10^3 Pa), no values were given in the text for the permeation. It is possible to assume that this omission was intentional to keep others from applying their values to beryllium materials where the oxide quality and thickness are unknown.

Anderl et al. [23] used 3 keV D_3 ions at beam densities of approximately 5×10^{19} D/$\text{m}^2\,\text{s}$ to measure the ion beam driven permeation of deuterium through 99.96% purity cast beryllium. The samples were 20 mm^2 with thicknesses of 25–71 μm. No permeation at all was seen for temperatures below 750 K. For temperatures slightly above this temperature, permeation fractions of less than 10^{-5} were recorded along with breakthrough times four orders of magnitude longer than predicted. The authors reported the upstream surface of the sample to have severe damage and pitting to a depth of 1 μm. This damage was listed as the probable cause of the low permeation rate. The long breakthrough time was credited to trapping.

Causey et al. [24] used lower energy particles (200 eV) but much higher fluxes (1.1×10^{21} T/m^2 s) in their measurements of hydrogen isotope permeation through 99.4% purity S-65 B beryllium. Sample thicknesses were varied between 51 and 254 μm while temperatures varied between 673 and 823 K. The permeation fractions of the implanted tritium were higher than those reported by Anderl et al. [23], falling between 5×10^{-6} and 2×10^{-4}. The rate of permeation did not properly scale with sample thickness. The final conclusion of the work was that the oxide layer on the upstream and downstream sides of the sample controlled the rate of permeation.

3.4. Implantation retention and surface effects

A very complete review of hydrogen isotope retention in beryllium due to implantation was completed by Anderl et al. [25] in 1999. Langley [26] performed some of the earliest implantation of hydrogen isotopes into beryllium. The beryllium used in the experiments was approximately 99.1% pure and was prepared by cold isostatic pressing followed by hot isostatic pressing. For 25 keV deuterium, he recorded nearly 100% retention until the particle fluence reached approximately 2×10^{22} D/m^2. Above this fluence, the retention flattened to a limit of about 2.8×10^{22} D/m^2. Wampler [27] performed similar experiments loading 99.6% purity cold and hot pressed beryllium to saturation with 500 and 1500 eV deuterium ions. Saturation in the implant zone occurred at about 0.31 D/Be. Thermal release experiments of saturated samples showed the retention to be controlled by 1 and 1.8 eV traps. Möller et al. [28] implanted polycrystalline sintered S65 beryllium samples with monoenergetic deuterium ions in the energy range from 60 eV/atom to 10 keV/atom at temperatures from room temperature to 920 K. Similar to the findings of Langley [26], post-irradiation examination of the samples showed oxidation of the surface, up to about 20 monolayers thickness even though the background pressure in the experimental chamber was maintained at 10^{-8} Pa. Also similar to the results of Wampler [27], saturation scaling linearly with particle range was noted.

In a latter set of experiments using low concentrations of deuterium in zone melt recrystallized single crystal beryllium, Wampler [29] recorded thermal release of the deuterium controlled by a 2.3 eV trap. When the samples were pre-bombarded with helium to produce bubbles into which the deuterium could agglomerate, the effective permeation out of the bubbles to the surface was seen to be seven orders of magnitude lower than the value calculated using published solubility and diffusivity data. In a series of experiments on deuterium retention in several metals, Haasz and Davis [30] reported a 0.39 D/Be saturation in the implant zone. During thermal desorption of the deuterium after implantation, most of the deuterium was released at about 500 K. Yoshida et al. [31] used 8 keV deuterium ions in their experiments with 99% pure powder metallurgy beryllium. Bubbles were seen to form for all temperatures examined between room temperature and 873 K. For temperatures above 573 K, large roundish bubbles formed at higher doses. The bubbles remained even after annealing at temperatures as high as 973 K, agreeing with Wampler's [29] data showing very low permeation from bubbles. In experiments on deuterium implantation into actively cooled beryllium monoblocks using very high fluences of ions, Falter et al. [32] also saw the saturation type behavior for beryllium. They compared their data for different temperatures and ion energies to others in the literature, and showed the saturation values to vary directly with the energy of the particles. Macaulay-Newcombe et al. [33] ion implanted 99% purity hot isostatic pressed beryllium samples at 298 K using 30 keV particles. They also used gas charging of the beryllium at 773 K using deuterium gas at a pressure of 13.3 kPa. Subsequent outgassing of the ion implanted sample showed release at about 710 and 820 K, agreeing fairly well with the earlier data of Wampler [27]. For the gas charging, relatively small amounts of retained deuterium were seen during desorption. Also, subsequent use of the same samples without annealing between experiments increased the amount of absorption and the temperature at which the gas was released. The oxide layer was seen to increase with each usage, possibly explaining the behavior.

There have been several experiments using lower energy hydrogen isotope ions on beryllium. Hsu et al. [34] looked at the transient release of deuterium immediately following implantation of Brush Wellman S-65 B beryllium using a Penning discharge. In these experiments, the sample was first heated to the desired temperature (333–800 K), and the discharge was then initiated. The particle flux was held at 7.4×10^{20} D/m^2 s with ion energies of 150 and 500 eV. The same sample was used for all experiments. For the experiments where the oxide layer was thought to be removed, the transient release followed a t^{-1} behavior. The integrated release increased steadily with temperature until it leveled off at 700 K. The average amount of released deuterium was about 10^{17} D/cm^2. Causey et al. [35] used very intense fluxes of 100 eV deuterium and tritium ions in their retention measurements in S-65 beryllium. In this case the flux was varied between 1×10^{21} and 2.8×10^{22} ions/m^2 s while the temperature of the measurements varied from 373 to 973 K. With the exception of the single point at 973 K, the retention decreased continuously with increasing temperature and was less than 3×10^{21} (D + T)/m^2 for all cases. Open porosity in the implant zone was listed as a possible reason for the low retention.

Similar retention values were seen in the experiments on S-65 B performed by Doerner et al. [36] using the PISCES experiment. They also listed open porosity in the implant zone as the cause of the lower than expected retention values. Sharapov et al. [37] used hot isostatic pressed beryllium containing 2.2% BeO in their deuterium accumulation experiments at 740 K. A plasma source with a heated cathode was used to provide atomic deuterium, and the sample was biased with a +80 V to limit the positively charged ions. They reported that the retention increased from 2×10^{20} to about 2×10^{21} D/m^2 as the fluence increased from about 6×10^{22} to 2×10^{24} D/m^2. Depth profiling of the samples showed the depth of penetration increasing from about 80–460 nm as the time of exposure went from 10 up to 240 min. They also reported the oxide layer to be growing at a rate of 0.4–0.5 nm/min.

A series of key experiments [38–40] in Russia provided the real understanding of the retention of hydrogen isotope implanted into beryllium. Chernikov et al. [38] and Alimov et al. [39] showed that hydrogen isotope retention is strongly affected by adsorption on bubble and cavity walls. According to Chernikov et al. [38], at 300 K tiny deuterium bubbles of a high volume density are formed at low fluences in 97.8% purity TIP-30 beryllium, but then progress to the formation of microchannels. Even when these microchannels intersect with the surface, the deuterium retention remains at or above 8 at.%. For irradiation at 500–700 K, small facetted bubbles and large oblate gas-filled cavities are formed. This microstructure extends beyond the range of the implanted ions. At 700 K, the concentration of deuterium is lowered to about 0.5–1.0% in the near-surface layer (0.5–1.0 μm). Alimov et al. [39] in their work using S-65B beryllium postulated that the retention in this porous region was due to trapping of deuterium atoms in radiation vacancies, deuterium adsorption on bubble and cavity walls, and the bonding of deuterium atoms to beryllium oxide present in the surface oxide layer and as metallurgical inclusion in the bulk. Markin et al. [40] looked at the thermal desorption of deuterium from ion implanted TIP-30 beryllium samples. At lower temperatures, the desorption occurred at two peaks (about 460 and 490 K). While the temperature location of the peaks did not depend on the ion fluence, the magnitude of each peak did depend on the ion fluence. There was also a higher temperature release of deuterium where the peak of the release rate increased from 850 to 1050 K as the ion fluence was increased, but ultimately returned to about 850 K as the fluence reached very high values. The lower temperature peaks were postulated to be due to the release from the network of opened channels and to the uncovering of bubbles/closed channels to the outer surface. The higher temperature peak was postulated to be due to liberation of deuterium atoms bound at immobile and stable vacancy complexes.

3.5. Tokamak results

While beryllium has seen limited use in other fusion reactors, the behavior of the hydrogen isotopes in the beryllium has been studied extensively for the JET device. Saibene et al. [41] used the test vessel at JET to determine the hydrogen recycling coefficient for beryllium. The beryllium for these experiments was a thick in situ deposited beryllium layer greater than 50 μm thick. An RF assisted DC discharge was used to generate hydrogen ion fluxes of approximately 9×10^{17} H/m^2 s with energies up to 1 keV. For temperatures between 373 and 523 K, the initial pumping of the hydrogen ions was very strong. At about 6–8 s into the discharge, the pumping action decreased rapidly but did not drop to zero even after 60 s. During the initial stage of the discharge, the pumping parameter, defined as $D/2K$, averaged about 4×10^{20} m^{-2}, similar to the values calculated for nickel and stainless steel. The authors stated that values this high for the pumping parameter suggest high diffusivity and relatively low recombination. Sartori et al. [42] used gas balance measurements in JET to examine the in-vessel retention of the hydrogen isotope fuel. They found that the amount of deuterium required to fuel the tokamak during the beryllium phase of JET was higher than that for the earlier carbon phase. Unlike carbon, continuous gas feeding was required to maintain a density flat top when beryllium was used. Additionally, after beryllium phase discharges, the measured release fraction was increased, indicating a higher dynamic retention during the discharge. It was noted that even a thin layer of beryllium on the carbon was sufficient to change the outgassing characteristics, suggesting that the retention was driven by surface effects. Ehrenberg et al. [43] examined pumping with beryllium in JET during the same time period as the above two references. They showed that the JET beryllium pumped approximately 10^{21} deuterium atoms/s at the beginning of the shot and then continued to pump at a slower rate over the next 10 s. That is compared to the carbon phase where much lower initial pumping was recorded with no pumping several seconds into the shot. After the shot was terminated, the beryllium outgassing rate was proportional to t^{-n} where $0.6 \leqslant n \leqslant 0.7$. This power law was obeyed from about 10 s after termination of the discharge up to about 1000 s. Integrating the outgassed molecules yielded recovery fractions of 30–70% of the amount pumped during the discharge. The authors argued that the release could only be explained if it were recombination limited. In 1994, Andrew and Pick [44] gave a more detailed model of the retention and release of the hydrogen isotope fuels from the JET beryllium.

They described the pumping action as due to a saturation effect over a very large fraction of the wall. The subsequent release after termination of the discharge was described as a detrapping process with subsequent recombination of the detrapped atoms.

3.6. Codeposition of beryllium with hydrogen isotopes

The codeposition of beryllium with hydrogen has been measured by Mayer [45] and by Causey and Walsh [46]. In the study performed by Mayer [45], the sputtered beryllium was produced by the impinging 0.1 mA of 4.5 keV D_3^+ ions onto a beryllium disk. The sputtered beryllium was collected on a silicon collector. While the vacuum in the apparatus was quite good (10^{-5} Pa), the relatively slow sputtering process resulted in the formation of a beryllium oxide layer instead of a beryllium layer ($O/Be \approx 1$). While this experiment (and the one by Causey and Walsh [46]) were perhaps intended to examine the codeposition of hydrogen isotopes with beryllium (or beryllium oxide), the reflection of the primary ions resulted in the formation of a coimplanted layer (for both experiments). In the Causey and Walsh [46] experiments, 1–3 A of 100 eV deuterons were used to sputter the beryllium. The much more intense sputtering rate of this experiment resulted in layers composed primarily of beryllium (O/Be levels varied between 0.03 and 0.125). The results for the two experiments are shown in Fig. 5. For the Mayer/BeO experiment, the results are similar to that for the codeposition of carbon and hydrogen. For the Causey–Walsh/Be experiment, the retention is significantly lower. The conclusion to be drawn from these experiments is that beryllium and hydrogen do not codeposit (coimplant) to form a hydrogen rich layer, but beryllium oxide and hydrogen do codeposit (coimplant). The difference is likely due to the chemical affinity of hydrogen and oxides.

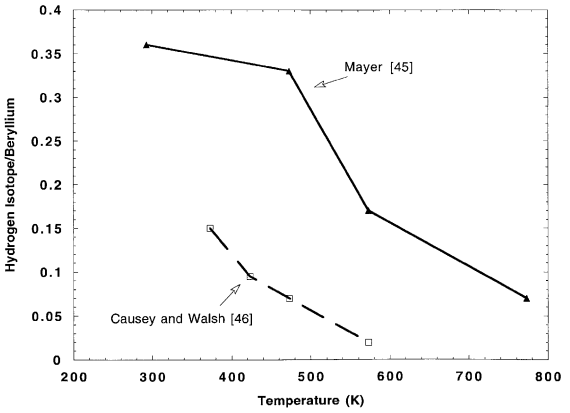

Fig. 5. Codeposition of hydrogen with sputtered beryllium.

3.7. Neutron production of tritium

One of the advantages of using beryllium in a fusion reactor is multiplication of the neutrons from the n, 2n reaction. Many blanket designs include beryllium for exactly this purpose. This reaction unfortunately has an effect on the swelling of the beryllium due to the immediate decay of the resulting Be^8 into two helium atoms. Of more importance to the discussion here is the n, a reaction that results in the production of He^4 and He^6. The He^6 quickly decays to Li^6. Li^6 subsequently absorbs a neutron to produce another helium atom and a tritium atom. It is these tritium atoms that can begin to dominate the tritium inventory in beryllium used in a fusion reactor. While the amount of tritium produced in the beryllium by this process varies with the neutron energy spectra, an estimate of the amount of tritium that will be produced in the fusion reactor environment can be estimated from the study by Baldwin and Billone [47]. In their experiments, a sample of theoretically dense beryllium was exposed to a neutron fluence of 5×10^{26} n/m^2 with 6% of the neutrons having an energy greater than 1 MeV. This irradiation resulted in 3×10^5 MBq/g (2530 appm) of tritium. Scaling these results to fusion reactor conditions, 50 Mg of beryllium in a blanket/first wall exposed to 3 MWy/m^2 fluence would generate as much as 5.5 kg of tritium.

In their experiments with neutron irradiated beryllium, Baldwin and Billone [47] used stepped anneals to examine the release of tritium for beryllium samples with different densities. Each sample would begin with a several hundred hour anneal at 773 K followed by long-term anneals at 100 K increments. At each new temperature, there was a non-diffusional burst followed by a steep drop in the release rate. While the behavior was similar for all three densities, the fractional release at each temperature was highest for the lower densities materials. The authors modeled the data by assuming a different diffusivity for each different density sample.

In a similar set of experiments, Andreev et al. [48] irradiated hot-pressed high density beryllium at 373 K. They performed thermal desorption spectroscopy of the samples with a heating rate of 10 K/s. The tritium release began to ramp slowly upward at about 773 K with a sharp peak located at a higher temperature. For the sample irradiated to 3×10^{25} n/m^2, the peak was centered at about 1080 K. For the sample irradiated to 1×10^{26} n/m^2, the peak was located at the lower temperature of about 1030 K. The authors noted considerable changes in the microstructure of the samples as the temperature progressed beyond 973 K. At 973 K, large number of pores with a diameter of 2–16 μm were formed. These pores had increased in size to 25–30 μm by the time the anneal passed through 1373 K.

Beryllium used in a D–T burning tokamak will produce tritium throughout the material by transmutation.

If the beryllium is maintained at a temperature below about 800 K, almost all of the tritium produced will be retained. Because of the limited uptake of tritium from the plasma by the beryllium, this transmutation produced tritium will quickly dominate the tritium inventory for a beryllium first wall.

3.8. Beryllium summary and conclusions

For an understanding of the behavior of hydrogen implanted into beryllium, the defining experiments are those performed by Anderl et al. [23] in 1992, Yoshida et al. [31] in 1996, and most importantly, the series of experiments in Russia [38–40] over the last five years. This combination of experiments, each building on the results of the earlier data, showed the development of connected porosity in beryllium samples exposed to energetic hydrogen isotope ions with the porosity extending beyond the range of the particles. Prior to these measurements, researchers examining the interaction of hydrogen with beryllium thought of beryllium in the same manner as they would think of hydrogen in metals such as nickel, iron, or copper. The normal assumption would be that hydrogen injected into beryllium would go into solution and diffuse throughout the metal. In reality, hydrogen's behavior in beryllium is closer to that of hydrogen in graphite (see the section on graphite). The very low solubility (perhaps almost zero) of hydrogen in beryllium prevents injected hydrogen from staying in solution in beryllium. After extensive bombardment, a honeycomb type of structure extending beyond the particle range develops. At least part of this structure is composed of beryllium oxide. At lower temperatures, this structure is able to retain approximately 0.3–0.4 H/Be [26,27,30], tied at least partially to the oxide. This behavior explains the initial strong pumping of hydrogen presented by newly exposed beryllium. It is this same porosity that is likely responsible for a sizeable fraction of the pumping seen during the later stage of the tokamak discharges. One only has to look at the honeycomb structure presented by Chernikov et al. [38] to understand its potential as a reservoir for stored gas. During the discharge, release of hydrogen from the saturated near-surface region provides a large excess of molecules that can flow either inwards or outward through the porosity. At the end of the discharge, the gas begins to come back out of the porosity, but the tortuous path out results in time constants in the 10s of seconds. A second possible mechanism of pumping during the discharge is the diffusion of atoms deeper into the material. Based on the results of experiments by Thompson and Macauley-Newcombe [18,19] and Wampler [29], it is postulated here that diffusion occurs along grain boundaries. The release of the atoms from these grain boundaries with their subsequent recombination add to that gas dumping back out of the porosity to prepare the beryllium for pumping during the next discharge.

Regardless of whether experimentalists finally perform the necessary experiments to determine the true form of hydrogen migration in beryllium, the behavior of beryllium in a tokamak is known. Any area where the beryllium faces the hydrogen plasma, the implantation results in open porosity. This open porosity becomes an excellent getter of oxygen and forms a thin honeycomb layer of beryllium oxide. The affinity of hydrogen to metal oxides results in substantial hydrogen uptake in this layer. The same is true of redeposited beryllium. In addition, there is gaseous uptake in the tortuous open porosity as well as inward migration perhaps into the grain boundaries. Beryllium's greatest problem for tritium inventory results from neutron irradiation. The neutrons will generate internal tritium that will accumulate over the lifetime of the material's use. After years of neutron exposure in a tokamak, inventories of the order of 5 kg are possible [47].

4. Tungsten

Tungsten is beginning to play a greater role in magnetic fusion energy as a plasma facing material. In the past, it has been used only sparingly due to the problem of excessive radiation losses in the plasma when tungsten is present in the plasma. Tungsten has been used selectively as a plasma-facing material in tokamaks, but usually only for experimental purposes. Tungsten's use in fusion devices will increase in the future. Tungsten has a very high threshold for sputtering as well as a high melting point. Applications of tungsten in areas where the energy of the plasma particles can be kept below the sputtering threshold (approximately 700 eV for tritium) [49] may remove the plasma impurity problem often associated with the use of tungsten.

4.1. Diffusivity

Diffusivity is a very fundamental property affecting the hydrogen isotope retention and migration in a material. There have only been a limited number of experiments to determine this parameter for tungsten, and many of those studies have been performed over a very limited temperature range. Fig. 6 shows the results [50–55] reported by the various experimenters for the diffusivity of hydrogen in tungsten. The most commonly accepted expression for the diffusivity is the one reported by Frauenfelder [50] in 1969. His diffusion coefficient is given by: $D = 4.1 \times 10^{-7} \exp(-0.39\ \mathrm{eV}/kT)\ \mathrm{m}^2/\mathrm{s}$. Frauenfelder measured the outgassing rate of hydrogen from saturated rolled sheet samples to determine the diffusivity of hydrogen in tungsten at temperature between 1200 and 2400 K. The nominal purity of his samples was

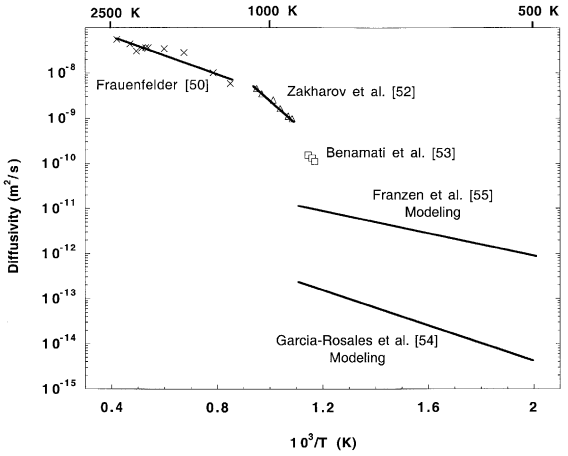

Fig. 6. Hydrogen diffusivity in tungsten.

99.95%. Over a somewhat smaller temperature range (1900–2400 K), Ryabchikov [51] also measured the diffusivity of hydrogen in tungsten, and reported values generally agreeing with those of Frauenfelder [50]. Zakharov et al. [52] used permeation techniques to determine the diffusivity of hydrogen in 99.9 wt% pure tungsten. These experiments were performed over the very limited temperature range of 900–1060 K. Their reported value for the diffusivity is: $D = 6 \times 10^{-4} \exp(-1.07 \text{ eV}/kT)$ m^2/s. Benamati et al. [53] also used gaseous permeation experiments to determine the diffusivity of deuterium in tungsten containing 5% rhenium. For the limited temperature range of approximately 850–885 K, the values determined for the diffusivity and permeability of deuterium in tungsten agreed with the Zakharov et al. [52] data. The authors did acknowledge that including trapping effects in their analysis and that of Zakharov et al. might result in both data sets agreeing with the earlier extrapolated results of Frauenfelder [50]. Garcia-Rosales et al. [54] reported the diffusion of deuterium in wrought tungsten during 100 eV D^+ ion bombardment to be best modeled by the expression: $D = 3.5 \times 10^{-11} \exp(-0.39 \text{ eV}/kT)$ m^2/s. Franzen et al. [55] modeled reemission, thermal, and isothermal desorption of deuterium from wrought and single crystal tungsten. Their expression for diffusion of deuterium in wrought tungsten is given by: $D = 1.5 \times 10^{-10} \exp(-0.25 \text{ eV}/kT)$ m^2/s. While the activation energy for the single crystal data was the same as that for the wrought tungsten, the pre-exponential of the single crystal expression was twice that of the wrought material. As both of the above modeling reports used multiple parameters to fit the release data, the values determined for the diffusivity are no more accurate than the values assumed for the other parameters including trapping and recombination rate coefficients.

4.2. Solubility

Fig. 7 shows the very limited solubility database [50,56] reported for tungsten. As with his diffusivity measurements, Frauenfelder [50] saturated 99.95% pure tungsten samples with hydrogen over the temperature range 1100–2400 K. His expression for this solubility is: $S = 9 \times 10^{-3} \exp(-1.04 \text{ eV}/kT)$ H/W atm$^{1/2}$. Mazayev et al. [56] examined the solubility of hydrogen in tungsten over a more limited temperature range (1900 to about 2400 K). At these higher temperatures, his measured solubility agrees very well with the measurements of Frauenfelder [50].

4.3. Gas-driven permeation

Frauenfelder [50], Aitken et al. [57], Zakharov et al. [52], and Benamati et al. [53] have all measured the gas-driven permeation of hydrogen through tungsten. All four reports list the permeation to be proportional the square root of pressure and to have an activation energy of 1.0–1.4 eV. The experiments performed at the higher temperatures [50,57] agree very well. The experiments performed at the lower temperatures [52,53] also agree with each other, but not with an extrapolation of the higher temperature work. It is possible that trapping affected the lower temperature results (at least the transient part of the experiments) but had no effects on the higher temperature experiments.

4.4. Recombination rate coefficient

Anderl et al. [58] used 3 keV D_3^+ ions on foils of reduction rolled, powder metallurgy tungsten with a pu-

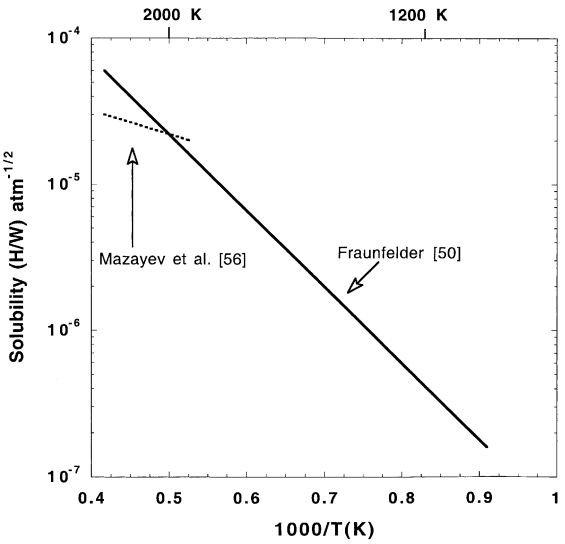

Fig. 7. Hydrogen solubility in tungsten.

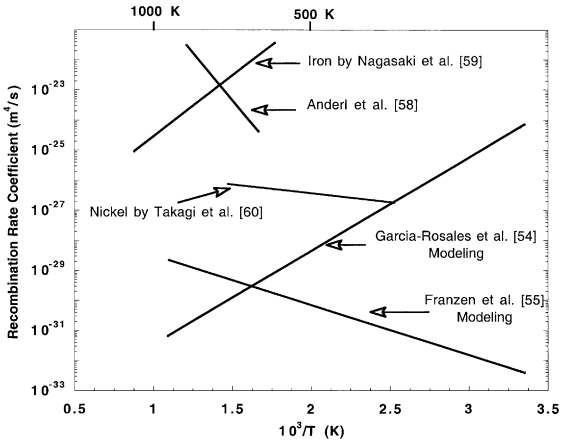

Fig. 8. Hydrogen recombination rate coefficient for tungsten.

rity of 99.95% to determine the recombination coefficient for hydrogen on tungsten. For measurements over the temperature range of 690–825 K, the effective recombination rate coefficient was reported to be: $K_R = 3.2 \times 10^{-15} \exp(-1.16\ \text{eV}/kT)\ \text{m}^4/\text{s}$. The recombination rate coefficient calculated from this formula is shown in Fig. 8 where it is compared to the values determined by Garcia-Rosales et al. [54] and Franzen et al. [55] using multi-parameter fits of experimental data (see below). To allow comparisons to data for other materials, recombination rate coefficients for iron [59] and nickel [60] are also shown in this figure. Causey et al. [61] used an intense flux of 8.8×10^{21} (D + T)/m^2 s ions at an energy of 100 eV in experiments of hydrogen isotope retention in high purity (99.99%) and lanthanum oxide doped powder metallurgy tungsten disks. The experiments were performed over the temperature range of 423–973 K. From the tritium retention data, it was determined that the release was not rate limited by recombination, implying a $C = 0$ boundary condition. In fact, the retention of tritium in the tungsten was so low that an additional condition of ion enhanced diffusivity in the implant zone was required to explain the lower temperature results. Similar low retention and rapid release was reported by Haasz et al. [62]. On the other end of the spectrum, relatively low recombination rate coefficients were reported by Garcia-Rosales et al. [54] and Franzen et al. [55]. Both reports used multi-parameter fits of various experimental data to determine the recombination rate coefficient, diffusivity, trapping density, and trapping energy for tungsten. Using their formula for hydrogen on tungsten at 500 K yields recombination rate coefficients of 10^{-29}–10^{-31} m^4/s. Examining all of the reports on recombination rate coefficients, it is difficult to justify these low values. Conclusions on the recombination rate coefficient are discussed later in Section 4.6.

4.5. Implantation retention and surface effects

Van Veen et al. [63] used 2 keV protons to examine the bonding of hydrogen to voids in single crystal tungsten. Thermal desorption of implanted hydrogen from single crystal samples containing 1 appm voids showed single broad desorption peaks centered at 600–700 K, with the higher temperature peak associated with the higher implantation fluence sample. The authors stated that the release of the hydrogen could be well modeled by the assumption of gas going back into solution from the voids and diffusing to the surface. The activation energy for the process was listed as varying from about 1.0 up to 1.4 eV with the higher apparent energy corresponding to later in the thermal desorption process where the pressure in the void has dropped. A small desorption component corresponding to an activation energy of 1.8–2.1 eV was categorized by the authors as chemisorption from the walls of the voids. In a subsequent study, Eleveld and van Veen [64] used thermal desorption spectroscopy after implantation with 30 keV D_2^+ ions to examine the interaction of deuterium with voids in tungsten. Samples with no voids irradiated to a fluence less than 1×10^{20} ions/m^2 released most of their deuterium at a temperature of 550–600 K. Pre-implantation with helium to create voids was seen to create a second desorption peak at approximately 650 K. As part of this work, the authors determined a value of 1.43 eV for the dissociation enthalpy of deuterium for vacancy type defects. Continuing their work, Eleveld and van Veen [65] examined single crystal tungsten samples exposed to increasingly high fluences of 30 keV D_2^+ ions. Only at fluences above about 10^{19} D/m^2 was a second desorption peak recorded at about 800 K. This peak was suggested to be due to the formation of voids containing 11–16 vacancies.

7.5 keV deuterons were used by Pisarev et al. [66] in a study of the low flux implantation into 99.94% pure rolled tungsten. Desorption peaks at 350, 480, 600, and 750 K were noted during thermal desorption. Annealing prior to implantation reduced the fraction of deuterium in the higher temperature peaks, and the highest temperature peak was only noted for the higher fluences.

In high fluence implantation studies of beryllium, molybdenum, and tungsten at room temperature, Haasz and Davis [30] compared the retention of 1 keV deuterium in the different materials. The 0.025 mm thick tungsten foil samples saturated at a retention of 6×10^{20} D/m^2 when the fluence reached 10^{22} D/m^2. Desorption experiments showed that the deuterium was released at two different temperatures with the higher temperature peak saturating first. Even though this higher temperature peak saturated in magnitude, it widened towards higher temperatures. In subsequent experiments, Haasz et al. [62] extended the measurements on deuterium implantation in tungsten to a series of higher temperatures,

added 300 and 500 eV implantations, added lanthanum oxide samples to their sample matrix, and pre-annealed all samples at 1473 K for 1 h. In a series of exposures at 500 K, the undoped tungsten samples did not saturate in retention at higher fluences. The lanthanum oxide doped samples did saturate, but at a fluence higher than that for the saturation of the room temperature exposed pure tungsten samples. Nuclear reaction profiling of both types of samples showed high concentrations of deuterium in the near-surface region, including depths well beyond the implantation zone. At the same 500 K and 1 keV, one tungsten sample was exposed to a series of exposures and desorptions. The deuterium retention was seen to increase with each cycle, suggesting an accumulation of traps or voids. For doped and undoped samples exposed to the same fluence of 10^{23} D/m^2 at 500 eV at different temperatures, the retained deuterium was seen to peak for exposures at temperatures close to 450 K.

Hundred eV deuterium implantation was used by Garcia-Rosales et al. [54] to investigate the trapping and release of deuterium in wrought and plasma-sprayed tungsten. Thermal desorption spectroscopy of the implanted samples showed two broad peaks at 475–612 and 670–850 K. The higher temperature peak was the smaller of the two peaks. Modeling of the data suggested two trap energies affecting the release characteristics. The authors stated that while most of the release at the lower temperature was due to diffusion, they believed a trap at an energy of approximately 0.85 eV also affected the amount of deuterium seen at this peak. The second peak was thought to be due to trapping at defects with an activation energy of 1.4 eV. For the different materials used in this study, the higher retention was recorded for the materials with the higher porosity.

Franzen et al. [55] used data from experiments on reemission and thermal and isothermal desorption of deuterium implanted into single crystal and wrought tungsten at energies from 100 eV up to 8 keV to produce a hydrogen/tungsten model. The model suggests a lower temperature trap at about 0.5 eV existing throughout the materials. A second trap at about 1.2 eV was thought to exist only in the implant zone and to be due to the implantation. This model also claims that the release of deuterium from the tungsten is recombination rate limited.

Macaulay-Newcombe and Thompson [67] implanted single crystal tungsten at 300 and 500 K with 20 keV D^+ ions. After implanting for 3 h at 300 K, approximately 67% of the deuterium had migrated out of the implant zone (released or diffused deeper into the sample). Heating the sample to 500 K for 1 h resulted in a subsequent loss of another 30% of the deuterium. Further heating to 700 K for 3.5 h resulted in most of the deuterium being transferred out of the implant zone, leaving a more or less constant 1000 appm deuterium concentration throughout the near-surface region. A similar implantation at 500 K resulted in only 8% of the deuterium remaining in the near-surface region. Heating to 700 K for 1.5 h left the concentration of deuterium at about 550 appm in the implantation zone.

Causey et al. [61] examined the tritium retention in samples of 99.99% pure tungsten and tungsten with 1% lanthanum oxide produced by powder metallurgy techniques. As listed in the previous section on recombination rate coefficients, the retention at the lower temperatures was so low, that even the assumption of $C = 0$ at the plasma–surface interface when combined with other 'accepted' values for the migration parameters significantly overpredicted the measured retention. It was concluded by the authors that the only explanation for the lower than expected retention was enhancement of the diffusion in the implant zone. Nuclear reaction profiling of samples exposed to deuterium only was combined with thermal desorption spectra of DT plasma exposed samples to determine the extent of trapping. It was determined that there were two traps, one at approximately 1.4 eV and another at 2.5 eV. It was postulated that the higher energy trap actually represented hydrogen isotopes recombined into molecules at defects and voids in the samples. The trapped density of the hydrogen isotopes averaged 400–500 appm and extended microns deep into the materials.

Alimov and Scherzer [68] used five different types of tungsten in their study of deuterium implantation and retention. 1.5 keV D^+ ions at a flux of 6.4×10^{18} D/m^2 s were injected into tungsten samples at 300, 600, and 900 K. Reemission, thermal desorption spectroscopy, and nuclear reaction analysis were all used to help understand the behavior of the deuterium in the samples. It should be noted that nuclear reaction analysis, which uses the detection of protons and αs produced by the nuclear reaction of energetic He^3 with deuterium, is only sensitive to the deuterium within the first few microns of the surface. Deuterium retention varied from a low of 2×10^{19} D/m^2 for the CVD and single crystal samples at 900 K up to a high of 4.5×10^{21} D/m^2 for the hot-rolled material at 300 K. The reemission approached unity most rapidly for the higher temperatures and for the single crystals. The thermal desorption spectra for the different materials were very different. The release from the single crystal, CVD, and inert gas plasma-sprayed tungsten samples were all characterized by the superposition of a peak at 400 K and another at 590–690 K. The release from the hot-rolled sample demonstrated a broad distribution peaked at 530 K with a gradual decrease over the temperature range of 700–1000 K. The release from the recrystallized vacuum plasma-sprayed tungsten sample reached a relatively sharp peak at about 350 K with some of the deuterium still being evolved as the temperature approached 1100 K. The amount of

deuterium recorded using nuclear reaction analysis of the samples implanted at 300 K was almost the same for all of the samples (about 3×10^{20} D/m^2). This amount was 2–20 times smaller than the amount measured by the other techniques, suggesting migration and trapping beyond the implant zone.

In a series of experiments using 6 keV ions implanted into double electron-beam zone refined single crystal tungsten at 300 K, Alimov et al. [69] used SIMS to examine the samples for both D atoms and D_2 molecules. Particle fluxes of approximately 4.5×10^{19} D/m^2 s and fluences as high as 10^{23} D/m^2 were used. Atomic deuterium was seen to be accumulated in the ion-stopping zone and at depths up to several microns. Molecules of deuterium were seen only in the ion-stopping zone.

In their study of deuterium transport and trapping in polycrystalline tungsten, Anderl et al. [58] attempted to determine the correlation between dislocation density on cell walls and deuterium trapping. The authors found that annealing the tungsten to 1673 K reduced the dislocation density on cell boundaries by about a factor of 7. A similar factor of 7 decrease in the trapping was determined by lag-time measurements of deuterium permeation. The trap energy was estimated to be 1.3–1.5 eV.

Komarov et al. [70] examined the deuterium retention in single crystal and polycrystalline tungsten exposed to deuterium plasmas. The deuterium ions striking the sample surface were a combination of 150 eV D_2^+ and D_3^+ ions with a flux of approximately 4×10^{20} D/m^2 s. The single crystal tungsten was the same as that used by Alimov et al. [69]. The polycrystalline tungsten was a powder metallurgy product, 50 μm thick, with a purity of 99.94%. The single crystal sample was exposed to the deuterium plasma for 2 h at 500 K and then thermally desorbed. Subsequent exposure of the same sample to the plasma after the thermal desorption resulted in less retention. After the third exposure of the sample to the plasma, the outer 2 μm of the sample was electrochemically removed prior to outgassing. No retention for the remaining sample was recorded. The polycrystalline tungsten sample was cut into four pieces after the plasma exposure. One sample had 2 μm electrochemically removed and another had 4 μm removed. During thermal desorption, deuterium was seen for all of the pieces, suggesting deep penetration of the deuterium into the sample along grain boundaries. The amount of deuterium registered for the single crystal sample on the first exposure was slightly greater than the amount seen for the polycrystalline sample even though the latter had deeper penetration. The measured amount agreed fairly well with that recorded by Haasz et al. [62], but was approximately one order of magnitude greater than that seen by Causey et al. [61]. Analysis of the data suggested the near-surface region of the single crystal sample had a D/W ratio of about 1.5% while the polycrystalline sample had a smaller ratio of about 0.4%.

Sakamoto et al. [49] examined the microstructural evolution in tungsten induced by hydrogen ion implantation. High purity (99.99%) single crystal and lower purity (99.9%) powder metallurgy polycrystalline samples were used in the study along with ion energies of 0.5–8 keV. The authors noted that the density of dislocation loops in the single crystal tungsten saturated at a low density when the temperature was 473 K and above due to the escape of dislocation loops by slip motion to the surface. They also noted that the saturation value for the dislocation loops was greater in the polycrystalline material. In both types of materials, hydrogen bubbles were seen only at temperatures of 873 K and above, even though it might be argued that the fluence of 10^{22} H$^+$/m^2 was too low for more production. It was also postulated that the enhanced dislocation loop density in the polycrystalline samples could have been due to impurities. In a subsequent study [71], the same authors examined the correlation between the microstructural evolution and the retention and desorption of deuterium. While the materials used in this study were the same as those in the earlier study, the energies were expanded to include 0.2–8 keV particles with the same maximum fluence of approximately 10^{22} D/m^2. Little difference was seen in the fraction of retained deuterium when the deuterium ion energy was shifted from 0.5 up to 8 keV. While the majority of the deuterium release was centered at 510 and 570 K, the 8 keV implantation resulted in the addition of another smaller peak at 710 K. The authors used this finding to conclude that the additional defects created by the higher energy did little to affect the trapping. Again, here the reader should note the very low fluence of 10^{22} D$^+$/m^2 used in this study. Holding the samples at room temperature for 148 h after implantation before thermal desorption shifted the release temperature to the higher values while reducing the amount of deuterium retained by up to 50%.

In a recent study, Haasz et al. [72] used 1.5 and 3.0 keV D_3^+ ions at fluxes in the range of $1–2 \times 10^{20}$ D$^+$/m^2 s to determine the effect of ion damage on the deuterium trapping in tungsten. Foils 25 μm thick with a purity of 99.96% were annealed at 1473 K for 1 h prior to the irradiation. For the 500 eV/ion implantation, fractional retention was noted to be increased by prior irradiation and thermal desorption. It was postulated that the effect was due to the creation of defect structures and voids that were not annealed away by the thermal desorption. The results were different for the 1 keV/ion implantation. In this case, it was found the retention for a fixed implantation fluence of 10^{23} D/m^2 was not affected by prior implantation and thermal desorption. The authors suggested the possibility of more displacements at the higher energy (even though this energy may have been too low to produce displacements) resulting in more

trapping in the very near-surface region. Most important in this report was the observation of large blisters (diameter of 10–50 μm) at high fluences of 500 eV deuterium ions. This observation was the first report of blisters in annealed tungsten exposed to hydrogen isotope ions with energies below that required to generate displacements.

Sze et al. [73] investigated the interaction of intense deuterium plasmas with lanthanum oxide doped tungsten and high purity (99.95%) tungsten foils (all unannealed). The doped samples exposed to the plasma at 850 K exhibited pits with diameters of several microns distributed over the entire sample surface. Sectioning of the samples showed the pits existing 5–10 μm deep into the material. Blisters were not present on the samples. Increasing the temperature of the exposure to 1250 K decreased the size and density of the pits. When the high purity foils were exposed to the same plasma conditions at 400 K, blisters with diameters of 10s of microns were seen. Elevating the exposure temperature to 1250 K eliminated all blisters.

Venhaus et al. [74] examined the effect of annealing on blister formation on tungsten. High purity (99.95%) foils and high purity (99.99%) powder metallurgy disks were exposed to 100 eV D^+ ions at a flux of about 10^{22} D/cm^2 s. Prior to plasma exposure, the powder metallurgy sample and one of the foils were annealed at 1273 K for 1 h. One foil was annealed at 1473 K for 1 h and another was left unannealed. Examination of the samples after plasma exposure revealed blisters on the unannealed and 1473 K annealed foils. The blister density was much greater for the unannealed sample. Both of the samples annealed at 1273 K did not exhibit blistering.

Very recently, Guseva et al. [75] exposed tungsten samples and several tungsten alloys to 150 eV deuterium ion fluxes of 7.7×10^{21} D/m^2 s for times sufficient to obtain particle fluences of 10^{25} D/cm^2 at 770 and 1370 K. No blisters were seen after the plasma exposure. Similar to the other experiments above using plasma exposures, the deuterium retention at 770 K was quite low, only slightly greater than 10^{19} D/m^2. For most of the samples exposed at this temperature, a small concentration peak was seen at the surface using elastic recoil detection analysis (in the first 50 nm). Beyond the surface, extending deep into the sample, the measured deuterium concentration was approximately 2000 appm, a factor of 4 or so greater than that measured by Causey et al. [61] in similar experiments. No deuterium was seen in the samples exposed at the higher temperature.

Mayer et al. [76] examined the codeposition of hydrogen with beryllium, carbon, and tungsten. The experimental results clearly demonstrated that tungsten does not codeposit with hydrogen, thus avoiding large tritium inventories in redeposited layers for DT burning devices.

4.6. Tungsten summary and conclusions

For the diffusivity of hydrogen in tungsten, the expression reported by Frauenfelder [50] should be used. Frauenfelder's experiments were performed at temperatures where trapping would have no effect on the hydrogen migration. Looking back at Fig. 6, it can be seen that the higher temperature measurements of Zakharov et al. [52] actually confirm the trend shown by the earlier work. As Zakharov's measurements were performed at lower temperatures where trapping might be expected to reduce the measured release rate, the data points begin to drop below Frauenfelder's curve, implying a higher activation energy. It would be a mistake to assume these lower temperature measurements to be more correct than those performed at the higher temperatures, especially since the measurements by Zakharov et al. [52] were only performed over a limited 150 K temperature range.

For the solubility of hydrogen in tungsten, the expression for solubility provided by Frauenfelder [50] should also be accepted as the best available. He used the reliable technique of saturating samples at high temperatures and relatively high pressures (approximately 1 atm), and then degassing them to measure the total uptake of hydrogen.

The recombination rate of hydrogen from tungsten is more difficult to quantify. There are two reports of very low values by Garcia-Rosales et al. [54] and Franzen et al. [55]. The coefficients derived by these researchers were based on multi-parameter fittings of retention and thermal release results. On the other hand, there are relatively high values reported by Anderl et al. [58] determined by fitting permeation data. In such a study examining steady state permeation, the number of parameters affecting the results is less than that for the above studies where retention and thermal desorption were analyzed. There are also the studies by Causey et al. [61] and Haasz et al. [62] providing low retention values that could only result from very rapid recombination at the sample surfaces. The earlier figure on recombination rate coefficients is reproduced here as Fig. 9 with the data for nickel and iron replaced by the calculations of the recombination rate coefficient predicted by the Baskes model [13] and the model given by Pick and Sonnenberg [12]. It should be noted that the assumption of a clean surface was used in both calculations. For the Baskes model [13] this means that the sticking coefficient, α, was set equal to 1.0. For the Pick and Sonnenberg model [12], this assumption means that chemisorption activation energy, E_C, was set equal to 0.0. It can be seen from this figure that the Baskes model [13] for tungsten agrees fairly well (in magnitude, but not slope) with the data of Anderl et al. [58], Causey et al. [61], and Haasz et al. [62] suggesting very rapid recombination at the surface of tungsten. The values calcu-

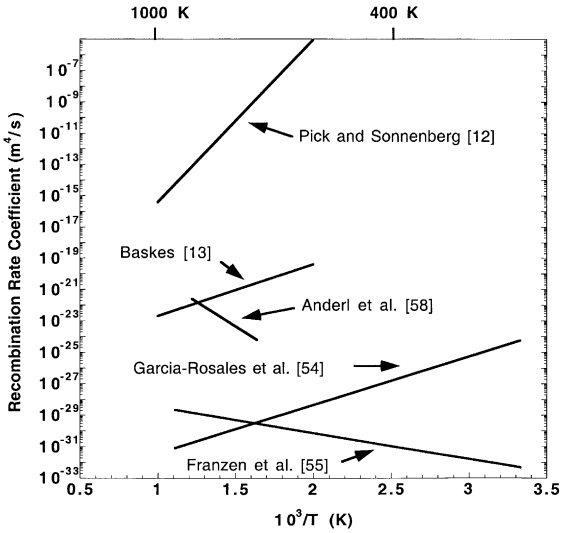

Fig. 9. Comparison of experimental and theoretical values for the hydrogen recombination rate coefficient for tungsten.

lated using the Pick and Sonnenberg model [12] are much larger than the other values, but overall magnitude is not so important in this case. Any recombination rate coefficient greater than about 10^{-22} m^4/s represents almost instantaneous recombination at the surface where diffusing concentrations are typical of fusion reactor conditions. Calculations to predict hydrogen isotope retention in tungsten will not significantly underestimate the retention if the boundary condition $C = 0$ (large K_R) is applied at all boundaries.

Examining the many papers referenced above on the release of implanted hydrogen isotopes from the different types of tungsten, peaks in the release rates are reported to occur at about 15 different temperatures over the temperature range of 350–1100 K. The temperature location of these release peaks appears to depend on material type, temperature of implantation, particle energy, flux, fluence and heating rate. To understand the different trapping mechanisms of hydrogen in tungsten, it is best to start with an understanding of single crystals first. A partial understanding of the multiple release peaks given above can be seen in the works of Tamm and Schmidt [77]. They showed that the different orientations of single crystal tungsten release absorbed hydrogen at multiple temperatures ranging from approximately 200 K up to almost 600 K (binding states varying between 0.6 and 1.6 eV). These results were for non-damaged, gas exposed single crystals. Eleveld and van Veen [64] examined the thermal desorption of deuterium from implanted single crystals and determined a dissociation enthalpy of 1.43 eV (released at 550 K) for the attachment of the deuterium atoms to single vacancies. Van Veen et al. [63] used positron annihilation to examine the occupation and desorption of hydrogen in voids created in single crystal tungsten by annealing samples previously irradiated with high energy protons and electrons. After the subsequent implantation with 2 keV H_2^+, the authors noted a broad release spectrum over the temperature range of approximately 400 up to 1200 K. The spectrum for a second sample irradiated to a higher fluence of 2 keV particles covered the same area but was centered at a higher temperature. The authors listed the cause of this shift as being due to filling voids at greater depths in the sample. Hydrogen diffusing to the surface from greater depths have to pass through areas where voids may recapture them. It is a form of trap controlled diffusion. The authors went on to discuss the pressure of hydrogen in the voids. They calculated the 350 K exposure to a fluence of about 10^{23} H$^+$/m^2 resulted in a hydrogen loading in the metal of approximately 5 appm and hydrogen in bubbles at a pressure on the order of 10 GPa. This pressure is approximately that required for loop punching. The dissociation enthalpy for the gas inside the bubbles was calculated by the authors to be almost exactly the same as that for hydrogen attached to single vacancies, 1.4 eV. They also calculated that hydrogen chemisorbed on the edges of the cavities to have a dissociation enthalpy of 1.8–2.1 eV.

Changing from single crystal to polycrystalline tungsten, the system becomes even more complicated. Anderl et al. [58] were able to show a strong correlation between sample annealing and permeation. The TEM analysis of the samples showed that the heat treatment at 1273–1673 K resulted in significant changes in the dislocation density for the cellular or boundary regions of the grains with no real effect on the cell interior defect density. A one-to-one correlation between removal of boundary dislocations and removal of traps was recorded. The conclusion to be drawn here is that a lot of the trapping is occurring at or near the cell boundaries. The energy calculated for these dislocation traps was the same as that calculated for vacancies, 1.4 eV. Venhaus and Causey [78] recently tried modeling the thermal desorption spectra of several earlier reports. Using $C = 0$ at the boundary, the diffusivity as given by Frauenfelder [50], and a single trap energy of 1.4 eV, the authors were able to reproduce almost every detail of each of the desorption spectra simply by varying the assumed trap density.

Other researchers such as Garcia-Rosales et al. [54] and Franzen et al. [55] have determined the presence of lower energy traps (0.5–0.85 eV). These traps may be associated with dislocations on grain boundaries, or they may be on the surface of the sample themselves. Regardless, these traps would be of interest only if the tungsten in the fusion reactor were operating at very low temperatures (below about 350 K).

The studies by Haasz et al. [72], Sze et al. [73], and Venhaus et al. [74] have demonstrated that hydrogen

isotope implantation into tungsten can definitely produce blistering. Many of the other studies such as those by van Veen et al. [63], Eleveld and van Veen [64,65], and Sakamoto et al. [71] have shown that hydrogen decorates pre-existing voids and can create new ones if they do not already exist. Deuterium implanted into tungsten will diffuse back to the surface or deeper into the material. The hydrogen diffusing deeper into the material will eventually find vacancies, dislocations, and voids into which they are trapped (unless the temperature is maintained at a temperature above which the 1.4 eV traps are thermally depopulated). If the temperature of the implantation is not very high, the hydrogen does not travel far away from where it is deposited. Creating areas of high pressure voids in the very near-surface region may create microcracks to release this hydrogen to the surface (note low retention values by Causey et al. [61] and Haasz et al. [62] at low temperatures). Increasing the temperature of implantation increases the diffusivity and therefore the distance the hydrogen can travel. Microcracks may still be created, but their density would be expected to be lower and the migration inwards of hydrogen would be greater. In this case, bubbles would be created deep into the material leading eventually to blister formation. At even higher temperatures, the traps no longer are able to hold the hydrogen, and the solubility of the tungsten is sufficient to keep all but the highest concentration of hydrogen in solution (note the decrease in retention in the studies of Causey et al. [61] and Haasz et al. [62] at temperatures above 700 K). It must be concluded that using tungsten in a plasma-facing application may eventually result in moderate inventories of hydrogen isotopes in the bubbles and blisters (unless the tungsten is maintained at very high temperatures). Note that the high ratio of released hydrogen isotopes to retained isotopes will require very long implantation times to generate this inventory. The bubble formation may also eventually result in tungsten being released into the plasma. Tungsten can be released into the plasma either through grain ejection (note the work of Sze et al. [73]) or by evaporation due to the creation of open blister caps that lose their thermal contact with the material below.

5. Carbon

Over the last two decades, carbon has been the material of choice for lining the walls of fusion devices. Carbon is a low Z material, has a low vapor pressure, has excellent high temperature properties, and is relatively inexpensive. The carbon materials used in fusion reactors are either graphites or carbon composites. The graphites used in fusion reactors are typically made using the Acheson process [79]. In this process, calcined coke is crushed, milled, and then sized. The size and shape of the resulting coke particles determine many of the properties of the graphite. After one or more additions of coal tar pitch and anneals at temperatures below 1200 K, the final graphitization process at temperatures between 2900 and 3300 K yields a graphite with relatively high porosity. These graphites normally have a density of around 1.8–1.9 g/cm^3 as compared with 2.25 g/cm^3 for theoretically dense graphite. This final product is composed of grains (typical size of 10 μm) with the grains further composed of graphite crystallites (typical size of 5 nm). Carbon composites are not greatly different from graphite. They are made by pyrolyzing a starting composite of carbon fibers in an organic matrix. These fibers have a high strength-to-weight ratio and are composed of almost pure carbon. As with graphite, the final product usually has density less than 2 g/cm^3. The porosity of the graphites and carbon composites plays a strong role in determining the behavior of hydrogen interacting with these materials. Because of the similarities between graphites and composites, distinction between the two in this review will only be mentioned when there are significant differences in their properties.

When hydrogen isotopes from the plasma interact with graphite or carbon composites lining the fusion reactor, there are four processes by which the hydrogen is retained in the carbonaceous materials. These four processes are saturation of the implant zone, codeposition with sputtered carbon on surfaces, absorption on internal porosity, and transgranular diffusion with trapping. Each of these mechanisms will be discussed in order.

5.1. Saturated layer

The retention of hydrogen in the carbon saturated layer has been reviewed in the past by Wilson and Hsu [80] and by Möller [81] and is discussed in numerous other publications. When a hydrogen atom is embedded into graphite (or carbon composite) at temperatures below about 800 K, it is effectively immobile [82–84]. It remains there until the surrounding conditions (e.g. temperature) are altered. Additional atoms are retained in the same manner until a saturation point is reached. Langley [85] used proton backscatter depth profiling of graphite implanted with 8 keV deuterons to examine the characteristics of the saturated layer. He noted that the concentration of implanted deuterium peaked near the end of range in the carbon at low particle fluences. As the fluence of particles increased, the peak height remained constant, but the peak width broadened with most of the growth back towards the surface. Eventually, a nearly flat profile was attained that was not altered by increasing the particle fluence.

The hydrogen to carbon ratio in the saturated layer is controlled by the temperature. This effect was nicely shown in work of Doyle et al. [86]. Their plot of frac-

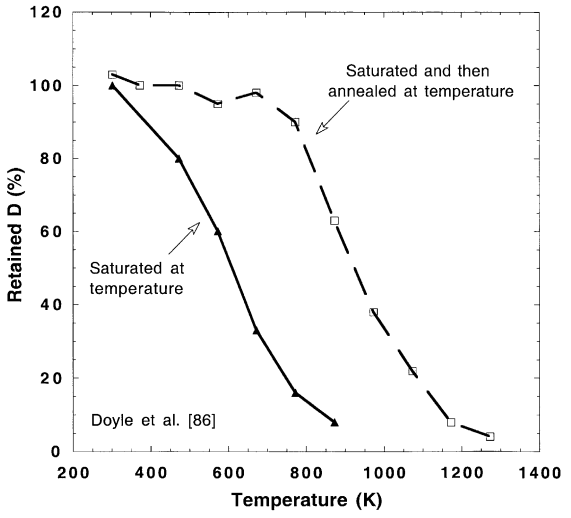

Fig. 10. Fractional retention versus temperature for the hydrogen saturated carbon layer.

tional retention versus temperature for samples implanted at temperature and for those annealed after implantation is shown in Fig. 10. Samples implanted with hydrogen isotopes at room temperature form this saturated layer with a hydrogen to carbon ratio of 0.4–0.5.

Niwase et al. [87] used transmission electron microscopy to show that the saturated layer is formed by converting the near-surface region of the carbon into an amorphous layer. Similar results were seen by Wright et al. [88] using Raman spectroscopy on graphite surfaces bombarded with 15 keV protons. Conjugated acetylenic bonds were noted in the amorphous layer. Gotoh and coworkers [89,90] used a combination of transmission electron microscopy and X-ray photoelectron spectroscopy to show that the crystallite size of their graphite decreased from 100 nm down to only 0.5 nm during implantation. The positive shift in the C1s line along with an increase in the interlayer spacing was suggested to be due to hydrogen–carbon bonding. Ashida et al. [91] combined SIMS with photoelectron spectroscopy to show that C–D and C_2–D (bridge bonds) were both formed in the saturated layer.

The saturated layer is extremely important when considering recycling of hydrogen plasma at the plasma/carbon interface, but insignificant when considering hydrogen isotope inventory in a carbon lined tokamak. When the hydrogen plasma is directed onto a saturated carbon layer, the recycling almost immediately goes to a value approaching 100%. If the carbon has been depleted of all hydrogen, the recycling coefficient begins near zero and changes over to a value close to 1 when saturation has again been achieved. The TFTR tokamak used helium fueled ohmic discharges to remove the hydrogen isotopes from the saturated layer of the carbon limiter to achieve the supershot confinement regime [92]. It was the active pumping by the limiter at the beginning of the discharge that reduced the inward transport of the low energy hydrogen back into the plasma.

As stated above, the saturated layer has a very limited effect on the tritium inventory for D–T burning devices. The reason for the minimal effect lies in the thickness of the layer. Unlike the codeposited layer (discussed below) which has no apparent limit on its thickness (unless it flakes off), the thickness of the saturated layer is determined by the range of the most energetic particles escaping from the plasma. This range dependence limits the thickness to only about 0.1 μm [93]. For a large fusion reactor with a plasma-facing area of 100 m^2 and a wall kept cool enough to maintain an H/C ratio of 0.4 (0.2 T/C for D–T), a total tritium inventory of 1 g will result. This amount may seem like a large quantity of tritium, but such a large tokamak will contain much larger inventories in the tritium systems and other locations in the carbon (codeposited layer and bulk trapping).

5.2. Codeposited carbon layer

When carbon atoms are sputtered from a graphite or carbon composite surface, a majority of these atoms are redeposited on the surrounding surfaces. As the sputtered atoms arrive at their new location, they are codeposited with energetic hydrogen isotope ions and neutrals. After their deposition, they are continuously bombarded with more of these particles until the thickness of the layer becomes greater than the range of the most energetic ions and neutrals. Those at the bottom of the layer are then protected from further bombardment. The key point here is that these energetic particles modify the structure of the redeposited layer. Some of the sputtered atoms chemically combine with other carbon atoms and with the hydrogen isotopes in the plasma prior to deposition. These 'molecules' are also deposited in surrounding areas, and may maintain higher H/C ratios if protected from further ion bombardment. For a more complete review of the characteristics of the codeposited layer and other similar coatings, the reader is referred to review articles by Winter [94,95], Vietzke and coworkers [96,97], Besocke et al. [98], Wilson and Hsu [80], Jacob and Möller [99], Reinke et al. [100], Jacob [101], and Coad et al. [102]. Similar to the saturated layer described above, the codeposited layer contain hydrogen at levels of 0.4 H/C (or higher in certain cases). Unlike the saturated layer, the codeposited layer can be quite thick. JET has reported codeposited layers on graphite tiles to be greater than 100 μm, and layers as thick as several mm (if flaking does not occur earlier) have been predicted for large devices such as ITER [103]. Such a layer in ITER would contain kilograms of tritium.

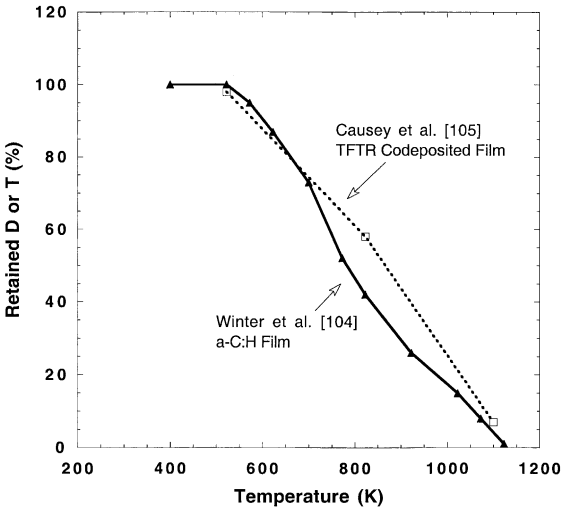

Fig. 11. Temperature dependence of the hydrogen isotope retention in an a-C:H layer and a TFTR codeposited layer.

Fig. 11 shows the temperature dependence of the hydrogen isotope retention in an a-C:H layer and a TFTR codeposited layer [104,105]. The similarity of these data to Fig. 10 for the saturated layer is apparent. As to the chemical composition of the codeposited layer, Dischler et al. [106] reported the hydrogen bonding to be pre-dominantly monohydride with sp^3, sp^2, and sp^1 in decreasing probability. Nyaiesh and Nowak [107] found their film to contain 25 at.% hydrogen with about 1/3 of it chemisorbed. Similar films analyzed by Angus et al. [108] were seen to contain 50 at.% hydrogen with part of the hydrogen unbonded. The fact that analysis of the same films one year later showed similar quantities of hydrogen was interpreted to mean that the unbonded hydrogen was strongly chemisorbed. In their study of carbon films produced by ion beam techniques, Nadler et al. [109] reported the sp^3 bonds to lose hydrogen and convert to sp^2 at around 773 K with the remaining hydrogen being released at about 973 K. Jacob and Möller [99] reported that increasing the ion energy of particles striking the film increases the C and H displacements, decreasing the H concentration. This higher energy increases the fraction of sp^2 bonding while decreasing the sp^3 bonding. This changing of the bonding removes most of the memory of how the film was originally produced (in their case, the type of precursor gas used for decomposition). Summarizing the above, the codeposited carbon/hydrogen layer is primarily amorphous, contains a large amount of hydrogen, has hydrogen bonded at several different types of sites, and has hydrogen that is chemisorbed on the carbon as well.

One of the most pressing problems for fusion reactors utilizing graphite or carbon composites as a plasma-facing material is how to remove the hydrogen isotopes from the codeposited layer once it is formed. For deuterium only devices, this removal is important from a density control point of view. For D–T burning devices, the tritium inventory is the driver for removing this component. From Fig. 11 it is apparent that maintaining or periodically heating the carbon surfaces to temperatures in excess of about 1100 K will prevent the buildup of hydrogen in the layer or remove it once it is there. Coad et al. [102] have recently shown some thick codeposited layers on tiles removed from a tokamak to be almost depleted of hydrogen isotopes. They claimed this depletion was due to thermal outgassing of the films when the limiters were heated to temperatures of about 1300 K by the JET plasma during high power discharges or by disruptions.

Another possible removal technique for the hydrogen in the codeposited layer is heating in air or oxygen [105,110–113]. A plot of the fraction of hydrogen isotopes remaining in a codeposited layer on a TFTR tile [105] and that remaining in a soft a-C:D film [110] is given in Fig. 12. It can be seen that the hydrogen is depleted much more rapidly when annealed in air than when annealed in vacuum (Fig. 11). Maruyama et al. [110] reported that part of the carbon reacts with the oxygen between 550 and 650 K releasing most of the deuterium. Haasz et al. [111] in similar measurements, reported the hydrogen release to occur in the form of water. Davis and Haasz [112] and Wang et al. [113] noted differences in the removal rate of hydrogen from films during annealing in air depending on the type of film. Films produced in tokamaks were the easiest to deplete of hydrogen, perhaps due to the metals also

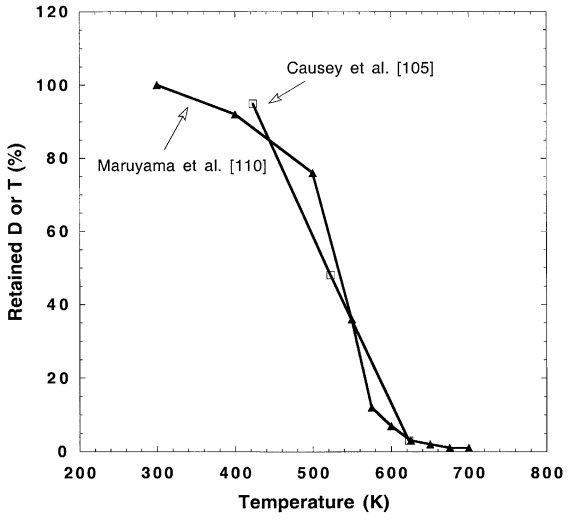

Fig. 12. Fractional retention of hydrogen in the codeposited carbon layer as a function of temperature when heated in air.

existing in these films. It was postulated that the metals may serve as a catalyst. Wang et al. also reported that the process of annealing in air leaves a layer saturated with oxygen. The remaining oxygen would pose a problem for subsequent operations in a tokamak.

Glow discharge cleaning and laser heating have also been proposed for the removal of the codeposited carbon/hydrogen layer. Hsu [114] examined glow discharge techniques using different gases for removal of the codeposited layer. While gases such as hydrogen, helium, and nitrogen were found to be effective at displacing the hydrogen isotopes in the near-surface region, only oxygen was able to partially remove the carbon, allowing removal of the hydrogen isotopes deeper in the codeposited layer. Cowgill [115] studied the use of helium–oxygen glow discharge to remove the hydrogen isotopes from thicker codeposited layers. He found the discharge to rapidly remove the hydrogen from the outer section of the codeposited layer, and to initially erode the carbon from the layer releasing even more of the hydrogen. Unfortunately, the normal incidence of the oxygen ions generated by the glow discharge created thin cones resembling grass or hair. Once the cones were formed, the erosion of the graphite slowed dramatically, significantly retarding the hydrogen isotope release. In addition to its limited ability to remove thick layers, the use of oxygen ions results in substantial uptake of oxygen in the graphite. Refke et al. [116] reported O/C levels as high as 0.25 in the near-surface region of the layer after implantation with 1–5 keV oxygen ions. This oxygen inventory would create severe problems for plasma operations after the cleaning process was completed.

Skinner et al. [117] recently reviewed the use of carbon dioxide or Nd:Yag lasers as a hydrogen isotope removal technique for the codeposited layer. Modeling predicted a multi-kW/cm^2 flux from such a laser with an exposure time of 10 ms would heat a 50 μm thick codeposited layer to 1000–2000 K. Even for short exposures, temperatures this high are very effective at removing the hydrogen isotopes from the layer, primarily in the form of hydrogen molecules.

Recently, examination of areas in JET [118] and in TFTR [119] have shown flakes exfoliating from surfaces. This finding is significant in that it shows that thick codeposited layers may detach themselves from the deposition area and allow the production of new layers. In addition, the flakes removed from the JET reactor contained total hydrogen isotope content exceeding the 0.4 H/C normally seen for these layers. von Keudell et al. [120] recently showed in experiments on codeposited layers where species such as CH_4, C_2H_2, and C_2H_4 were used as the feed gas that layers with a hydrogen to carbon ratios greater than 1.0 could be obtained. The JET flakes included protium which may have been absorbed as water vapor after removal from the machine.

5.3. Absorption on internal porosity

Graphites and carbon composites are porous materials. Most have BET surface areas of 0.25–1.0 m^2/g [121]. The porosity is created in all stages of the graphite and composite production due to misfits of the grains, gas evolution during heat treatment, porosity in the grains and fibers, and differential thermal contraction during the cooling process [79]. There are as many as 10^{15} pores/m^3 with pore diameters varying between 1 nm and 1 mm.

An excellent demonstration of the extent of the porosity in graphite was performed by Kiyoshi et al. [122]. In this experiment, 1 mm thick circular disks of T-6P isotropic graphite were used as permeation membranes. At all temperatures from 293 to 983 K, exposing one side of a graphite disk to either hydrogen or argon resulted in almost immediate flow of the gas to the other side. The authors suggested the permeation to be simple molecular flow. They did note that pre-annealing the samples increased the permeation rate, but this effect was postulated to be due to water removal from the pores, making more room for molecules to pass through.

It was this porosity that confused many researchers during the first exposures of graphite to hydrogen plasmas. Expecting to see only saturation of the implant zone, Flaskamp et al. [123] used a thermal atomic flux of hydrogen containing a tritium tracer to measure the retention of hydrogen in EK87 graphite. Instead of rapidly reaching equilibrium retention in the very thin implant zone, the retention continued to rise even after the particle fluence exceeded 5×10^{24} atoms/m^2. Unknown to the researchers, they were simply loading more and more of the pore surfaces with hydrogen isotopes as the implantation increased. Direct proof of the absorption of hydrogen isotopes deep into graphite was seen in a set of experiments performed by Causey et al. [124]. Dissolution profiles of POCO AXF-5Q graphite samples exposed to a deuterium–tritium plasma at 573 and 773 K revealed tritium at depths far greater than the range of the 100 eV ions. For the sample exposed to the plasma at 573 K, the tritium penetrated to a depth of about 0.3 mm, but the 773 K sample had measurable quantities of tritium at a depth of 2 mm. Confirmation of deep penetration of hydrogen in graphite was also given by Strehlow [125] in 1986 and later by Emmoth et al. [126] in 1990. Strehlow's experiments were performed at 1023 K using tritium gas. Mechanical sectioning of the samples after 4 h exposures showed deep penetration (beyond 0.15 mm) of tritium in H-327 graphite (substantial open porosity) but almost no penetration into CGB graphite (highly impregnated with little open porosity).

It is apparent from the experiments of Kiyoshi et al. [122] that hydrogen can easily access the graphite porosity. For absorption to occur on the porosity, the

molecules of the hydrogen must first dissociate. The dissociation can be achieved by high temperature as demonstrated in the experiment listed above by Strehlow [125] or by using a plasma to expose the graphite as demonstrated in the experiment of Causey et al. [124]. Dissociation can also be achieved by the use of a metal catalyst [127]. Barrer [128] studied the absorption of hydrogen on diamond and graphite and reported the activation energy for chemisorption to increase from 0.96 to 1.47 eV as the fractional coverage of the surface increased from 0 to 0.3. Thomas [129] reported the activation energy of hydrogen chemisorption on graphite to increase from 0.43 to 1.43 eV for coverages between 0.1 and 0.3. In a similar type of experiment using purified graphite, Bansal et al. [130] recorded four different energies for the chemisorption of hydrogen and postulated a fifth. These energies were 0.25, 0.36, 0.80, 1.32, and 2.17 eV. The purpose of reporting these data is to show that hydrogen absorbs on carbon surfaces at different types of sites with multiple or continuous activation energies. The values of the activation energies lie between 0.2 and 2.2 eV. Once absorbed, the hydrogen then migrates by jumping from one of these activated sites to another.

The effective diffusion coefficient for hydrogen on graphite surfaces has been measured by several groups. Robell et al. [131] used data on the uptake of hydrogen on platinized carbon between 573 and 665 K to infer an activation energy of 1.7 eV for the diffusion. Olander and Balooch [132] used a similar technique to determine an effective diffusivity for both basal and prism planes on carbon. They reported $6 \times 10^{-9} \exp(-0.66 \text{ eV}/kT)$ m^2s for the basal plane and $6 \times 10^{-11} \exp(-0.38 \text{ eV}/kT)$ m^2s for the prism plane. Causey et al. [124] used the measured tritium profiles in POCO AXF-5Q graphite tiles removed from TFTR and subsequently exposed to a plasma to report $1.2 \times 10^{-4} \exp(-0.9 \text{ eV}/kT)$ m^2s as the effective diffusion coefficient for hydrogen on graphite pores.

Excellent examples of tritium that has migrated deep into graphite and carbon composites along pore surfaces have been reported by Penzhorn et al. [133] in recent measurements of tritium in tiles removed from the JET fusion reactor. Mechanical sectioning followed by oxidation was used to determine the diffusion profiles of the tritium. Tritium at relatively high concentrations was detected 10s of mm deep into the tiles.

It is pertinent at this point to assess the importance of hydrogen isotope absorption and migration on pore surfaces as far as inventory is concerned. An upper limit to the hydrogen retention should be a monolayer coverage of all of the pore surfaces. For 1 m^2/g specific surface area typical of nuclear grade graphites, this coverage would result in 2×10^{25} atoms/m^3, or about 2 g for a 20 m^2 carbon wall that is 10 mm thick. Not only is this amount a relatively small quantity of hydrogen as compared to the codeposited layer, but it is also impossible to obtain. For temperatures sufficiently high to get inward migration of the hydrogen into the graphite pores, the temperature is too high to permit monolayer coverage of the pore surface. Thus, it may be concluded that the retention and migration of tritium on the porosity of graphite will never lead to high inventories. Still, for the decontamination of tiles used for relatively short times in tritium environments such as those for JET and TFTR, this deeply deposited tritium presents special problems for removal.

5.4. Diffusion, solubility, and trapping of hydrogen in graphite

5.4.1. Diffusion

Many people have attempted to measure the diffusivity, solubility, and trapping of hydrogen in graphite with large variations in the reported answers. The variations are due to the different experimental techniques used, the different types of graphites used in the studies, and the different analytical techniques used to extract the coefficients from the data. There has typically been an attempt to model the migration of hydrogen through graphite using standard concepts of diffusion with trapping. That approach will be followed here even though it is almost definite that hydrogen does not go into solution in the graphite crystallites. That argument will be discussed at the end of this section.

The reported values for the diffusivity of hydrogen isotopes in graphite are shown in Fig. 13. Rohrig et al. [84] used the release rate of tritium from nuclear graphites during isothermal anneals to determine the

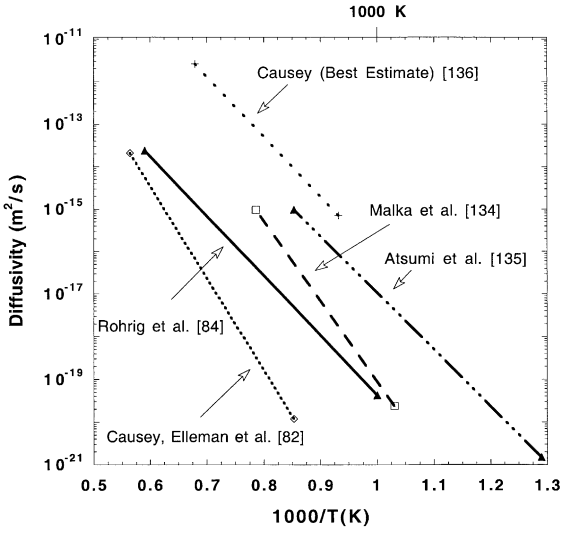

Fig. 13. Hydrogen transgranular diffusivity in carbon.

diffusivity of tritium in graphite. Their results were corrected to reflect the grain size as the real diffusion distance required to allow the release. Their reported diffusion coefficient is $D = 4 \times 10^{-6} \exp(-2.78 \text{ eV}/kT)$ m^2/s. Malka et al. [134] used a nuclear grade graphite with tritium produced in the material by neutron activation of lithium impurities. They reported the diffusivity to be given by $D = 8.3 \times 10^{-1} \exp(-3.8 \text{ eV}/kT)$ m^2/s. Causey et al. [82] used a recoil injection technique to measure the effective diffusivity of tritium in laminar pyrolytic carbon. Measuring the rate of tritium release from the pyrolytic carbon during isothermal anneals, the expression $D = 3.3 \times 10^{-2} \exp(-4.3 \text{ eV}/kT)$ m^2/s was determined. Atsumi et al. [135] used the rate of desorption of deuterium gas from graphite samples exposed to gas at elevated temperatures to determine the effective diffusivity. Their expression for the diffusivity is $D = 1.69 \times 10^{-4} \exp(-2.6 \text{ eV}/kT)$ m^2/s. An alternative value for the effective diffusivity was proposed by Causey [136] using data on the inward migration of tritium into POCO AXF-5Q graphite. He argued that the uptake of tritium in graphite is determined by the product of effective diffusivity times effective solubility. The uptake data were analyzed assuming the expression given by Atsumi et al. [135] for the solubility was correct. The expression determined by this technique (referred to in the figure as 'best estimate') is $D = 9.3 \times 10^{-5} \exp(-2.8 \text{ eV}/kT)$ m^2/s. The term 'best estimate' is used because the expression for the diffusivity is based on all earlier results with an increasing understanding of the migration of the hydrogen isotopes in the carbon bulk. It should be noted that the diffusion coefficients reported here pertain to the diffusion into the individual grains of the graphite, not the thickness of the graphite itself. The open porosity effectively makes it possible for each individual grain in the graphite to be exposed to the hydrogen gas.

5.4.2. Solubility

Atsumi et al. [135] determined the solubility of deuterium in ISO 88 graphite at temperatures between 1123 and 1323 K using gas pressures between 2.5×10^2 and 1.3×10^4 Pa by measuring the pressure change in a constant volume chamber. The expression for their solubility is $S = 6.4 \times 10^{-5} \exp(+0.2 \text{ eV}/kT)$ atom fraction/$atm^{1/2}$. This solubility is shown in Fig. 14 along with two data points determined by Causey [136] for POCO AXF-5Q graphite at 1273 and 1473 K with 1 atm gas pressure. Both data sets show a negative heat of solution, suggesting bonding of the hydrogen to the carbon.

5.4.3. Trapping and radiation effects

Causey et al. [124] exposed POCO AXF-5Q graphite to deuterium/tritium gas at high temperatures to examine the kinetics of the absorption process. For temperatures above 1500 K and 1.5 h exposures, it was discovered that increasing the pressure from 0.66 to 66 Pa did not increase the retention. This result confirmed the possibility that the high temperature retention was being controlled by trapping. Analysis of the data gave a trap energy of 4.3 eV with a density of 17 appm. Since the time of that report, there have been many experiments on the trapping of hydrogen isotopes in graphite and carbon composites and the effects of radiation on that trapping. In 1992, Atsumi et al. [137] reported that neutron irradiation was able to increase the apparent solubility of deuterium in graphite by a factor of 20–50. The radiation effect saturated at about 0.3 dpa. They also noted a decrease in the apparent diffusivity. In a later study, Atsumi et al. [138] noted that different graphites and composites could vary in their hydrogen retention values by as much as a factor of 16. The authors also noted a correlation of retention with lattice constant or crystallite size. Radiation damage was seen to decrease the crystallite size and increase the trapping. Wampler et al. [139] used 6 MeV C^+ ions to simulate neutron damage to different graphites. They found the effect of radiation damage on hydrogen retention to saturate at about 0.04 dpa. At this level of damage, the retention of deuterium in the gas exposed samples saturated at about 650 appm. In a subsequent study, Causey et al. [140] examined N3M graphite samples that had been neutron irradiated to 10 dpa at 873 and 1148 K. The sample irradiated at 873 K had a tritium trap density of 1800 appm, but this value was reduced almost by a factor of 5 in the sample irradiated at the higher temperature. In yet another study, Causey et al. [141] looked at tritium uptake in unirradiated and irradiated

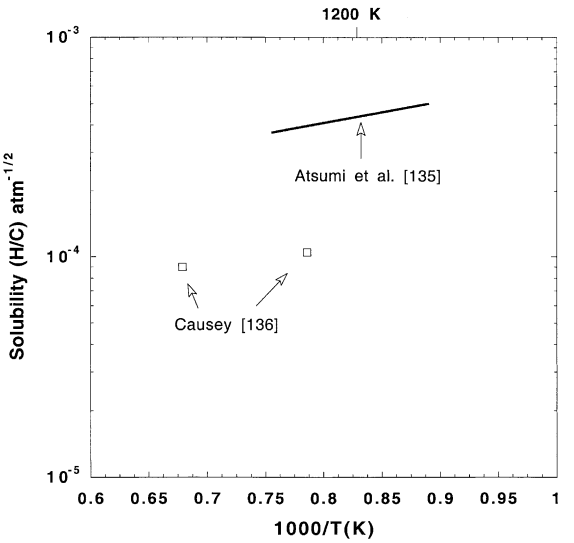

Fig. 14. Hydrogen solubility in carbon.

carbon composites. The pitch based carbon fiber composites used in this study both had large lattice parameters due to the sheet-like configurations of their fibers. Both of these composites retained less tritium before and after irradiation than other carbon materials studied in the past. It was proposed in the report that the lower retention was due to the fact that hydrogen is trapped on the edges of the crystallites which these materials minimized by their sheet-like makeup.

An alternative explanation of the hydrogen migration process in graphite was proposed by Kanashenko et al. [142]. They proposed that the hydrogen–graphite interaction is based on the adsorption of hydrogen on different types of sites in the graphite lattice. The first type of site is the edge carbon atoms of interstitial loops with the adsorption enthalpy of -4.4 eV/H_2. These sites are located between the graphite layers and may be kinetically limited at low temperatures due to the transgranular diffusion required to access them. The second type of site is the carbon network edge atoms with an adsorption enthalpy of -2.3 eV/H_2. These sites are more easily accessed because they are located on the grain surfaces connected to the surface through the porosity. The third type of site is the basal plane adsorption sites with an adsorption enthalpy of $+2.43$ eV/H_2. This site can be thought of as a third trap site or as the true solution. Either way, very few of these sites are occupied due to the high positive value for the enthalpy. Langmuir type of adsorption is proposed for all of the different sites. The density of the 4.4 and 2.3 eV sites are 20–200 appm respectively. They propose that radiation damage increases these sites to densities of 1500 and 5000 appm. While this work examined graphite from a different perspective, it confirmed rather than negated earlier work in the area of hydrogen migration and radiation effects on trapping.

5.5. Effects of graphite dopants on retention

Graphites doped with boron, silicon, and iron have been tested for use in fusion reactors as a way of reducing the sputtering. For hydrogen isotope retention characteristics, Alimov et al. [143] found an enhancement of the ratio of D_2 to CD_4 in the thermal desorption of bulk-boronized graphite implanted with deuterium at high fluences. They also saw a downward shift in the desorption peak maximum by about 200 K for the doped material. This shift was suggested to be due to a smaller binding energy for the absorbed deuterium. In their study of dopants, Haasz and Davis [144] found doping graphite with silicon, tungsten, boron, and titanium somewhat increased the retention of deuterium at high fluences. The thermal desorption spectra showed the dopant to lower the temperature of release and to cause multiple desorption peaks. Mayer et al. [145] found that graphites doped with boron, silicon, and titanium tended to retain more deuterium than undoped graphites when exposed to deuterium ions at room temperature. The increase was not dramatic. Causey et al. [146] compared the tritium retention in a doped graphite to that of undoped graphites for the case of high temperature exposure to gas. Over the temperature range of 1273–1473 K, the tritium retention in the USB-15 graphite (containing 15% boron) was 5–10 times lower than that for MPG-8 and POCO AXF-5Q graphites. The two undoped graphites had densities and pore structure similar to that of the doped graphite. The authors speculated that boron may be occupying the chemically active sites that would normally trap the hydrogen isotopes. In a similar study, Hirooka et al. [147] compared the tritium retention in three graphites at temperatures from 1073 to 1473 K after exposure to tritium gas. One graphite was undoped, one graphite contained 3 wt% boron, and one graphite contained 10 wt% boron. The tritium retention was inversely proportional to the boron content.

5.6. Carbon summary

Graphite and carbon fiber composites present several problems as far as hydrogen retention is concerned. The saturated layer will be present on all graphite surfaces facing the plasma. The only exception will be areas heated to temperatures in excess of about 1200 K during plasma discharges. The saturated layer will dominate recycling, but will have almost no effect on inventory due to its very limited thickness. It is possible to deplete the saturated layer between plasma discharges by the use of helium glow discharge to get pumping at the beginning of the next discharge. The codeposited layer has an almost limitless ability to store hydrogen isotopes in a carbon lined fusion device. This layer is extremely difficult to remove, and most removal techniques (heating in air, helium oxygen glow discharge, laser sweeping, etc.) leave residues such as oxygen or require long times to be effective. The surface connected porosity in a typical graphite or composite makes hydrogen available for absorption at all depths throughout the carbon materials. This openness then leads to possibly high tritium inventories by trapping at high energy traps sites, especially after neutron irradiation. Dopants tend to reduce this high energy trapping. The uptake of hydrogen isotopes in the bulk of the graphite at elevated temperatures can be predicted using expressions for diffusivity, solubility, and trapping with the effective diffusion distance being the grain size of the graphite or composite. The expressions for solubility and diffusivity as given by Atsumi et al. [135] and Causey [136] are recommended in that they are based on an understanding of the migration processes of hydrogen in carbon and take earlier experimental results into consideration.

6. Liquid metals

Liquid metals are again being given serious consideration as plasma-facing materials by the fusion community. The primary reason for this consideration is the excellent heat transfer capability of the liquid metals, a requirement for the removal of heat from a high-power density fusion reactor. At present, lithium, tin, and gallium are the primary candidates for use as plasma-facing materials. Tin–lithium, with a vapor pressure lower than that of lithium alone, is also being considered, but so little is known of its hydrogen retention characteristics, that it will not be discussed here. The hydrogen isotope migration parameters for lithium, tin, and gallium are discussed below.

6.1. Diffusivity

Moriyama et al. [148] used a capillary method to determine the diffusivity of tritium in liquid lithium. Their experiments determined the diffusivity to be given by $D = 8.56 \times 10^{-12}\ T/\mu$ m^2/s where T is the absolute temperature and μ is the viscosity of the liquid lithium. The authors quoted Shpil'rain et al. [149] for the viscosity, μ, of lithium to be given by $\log \mu = 1.4936 - 0.7368 \log T + 109.95/T$. Buxbaum and Johnson [150] also measured the diffusivity of tritium in liquid lithium. Their values were slightly lower (about a factor of 4) than those measured by Moriyama et al. [148], but had the same slope. Alire [151] examined the diffusivity and solubility of hydrogen in liquid lithium by examining the consumption of hydrogen in lithium and the Nb/Zr container in which it was held. This experiment, which required corrections for the transport through the container, determined that the diffusivity of hydrogen in lithium between 898 and 1178 K to be $D = 1.3 \times 10^{-3} \exp(-1.09\ \text{eV}/kT)$ m^2/s. These results are in strong contrast (much higher activation energy) to the results of Moriyama et al. [148] and Buxbaum and Johnson [150]. It is almost certain that the diffusivity through the container and release from the container surface into the lithium strongly affected the results.

It should be noted that the values determined by Moriyama et al. [148] and Buxbaum and Johnson [150] for the diffusivity are much higher than those for solids. The diffusivity lies close to 10^{-8} m^2/s for all temperatures between the melting point and 1000 K. The high mobility is significant in that it makes it almost impossible to achieve high localized tritium concentrations in the liquid metal. Even at fluxes of 1 A/cm^2, the tritium concentration at the end of range cannot rise above about 2% (based on calculations using the TMAP [152] computer code). The limited concentration should reduce the rate of production of lithium hydride (which only forms when the hydrogen concentration exceeds a few atomic percent), and reduce the chance of bubble formation in the liquid.

There appear to be no data available on the diffusivity of hydrogen in tin or gallium. An approximation for the diffusivity is given by Cussler [153] who generalized that the diffusivity of any solute in any liquid solvent is constant at approximately 7×10^{-10} m^2/s. This value is lower by a little less than an order of magnitude than the values reported in the above paragraph for liquid lithium, and should serve as an approximation until additional experiments are performed.

6.2. Solubility

For a phase diagram of the Li–LiH system, the reader is referred to Hoch [154]. Basically, at higher temperatures there is a single liquid present which disproportionates into two liquids (Li and LiH). Above 454 K but below 958 K, there is a two phase region composed of liquid lithium and solid lithium hydride. Examination of the phase diagram leads to the conclusion that very large amounts of hydrogen can be incorporated into a layer of liquid lithium. The implications of the large capacity to the behavior of plasma wall interactions in a fusion reactor are demonstrated in the next section on ion implantation.

Several researchers have determined the solubility of hydrogen isotopes in liquid lithium. Katsuta et al. [155] determined the inverse of the solubility to be given by the expression $\log_{10} K_T[\text{Torr}^{1/2}/(\text{H/Li})] = 3.86 - 2.32 \times 10^3/T$ from about 700 K up to about 900 K (the alternative expression is $K_S = 3.8 \times 10^{-3} \exp(+0.46\ \text{eV}/kT)$ (H/Li)/atm$^{1/2}$). Veleckis et al. [156] also determined the solubility of hydrogen in liquid lithium. For temperatures between 993 and 1176 K, their expression for the solubility is given by $K_S = 1.5 \times 10^{-3} \exp(+0.53\ \text{eV}/kT)$ (H/Li)/atm$^{1/2}$.

Iwase [157] reported very low hydrogen solubilities for tin. The solubility varied from 0.47×10^{-4} H/Sn at 673 K up to 1.54×10^{-4} H/Sn at 1278 K. Even though no definitive data are available on the hydrogen solubility in gallium, Mueller et al. [158] compare it to boron and indium to conclude that the solubility is negligible. Gallium forms a hydride, but it is only formed in special conditions in the laboratory.

6.3. Ion implantation

There are no references on the interaction of hydrogen ions with gallium. Erents et al. [159] used a mass analyzed 18 keV deuteron beam to examine the interaction of energetic hydrogen isotope ions with solid and liquid lithium. While conflicting results were obtained for the solid phase, the liquid phase with a clean surface resulted in 97% retention of the implanted deuterium for ion fluxes between 2.5×10^{18} and 2.5×10^{19} ions/m^2 s.

The fractional retention was seen to drop as temperatures exceeded 680 K.

In experiments just completed using the PISCES experiment, Baldwin and Doerner [160] have reported deuterium retention measurements showing almost 100% retention of all implanted deuterium even at the extremely high fluxes possible using this linear plasma device. As this report had not yet been published when the present paper was written, few details are presently known.

7. Conclusions

When selecting the materials to use for plasma-facing applications in a fusion reactor, the hydrogen isotope retention and recycling properties of the materials must be considered. For present-day devices without tritium, the hydrogen recycling properties of the material are probably more important than the hydrogen retention properties. The current tokamak operator desires a material that will temporarily retain the implanted hydrogen isotope during the discharge, preventing the return of the cold gas back into the torus where it will lower the plasma temperature. As plasma burn times become longer, recycling will become less important. As deuterium is replaced by a combination of deuterium and tritium, retention replaces recycling as the important parameter. From this review, it can be seen that each material presents the fusion designer with unique hydrogen isotope retention and recycling properties.

The ability of beryllium to pump hydrogen isotopes for short times in a fusion reactor environment appears to be due to the open porosity generated in the near-surface region [38]. It is likely that a combination of atomic absorption on the beryllium/beryllium oxide pore surfaces and molecular accumulation in the porosity accounts for a majority of the temporary holdup of the hydrogen isotopes in beryllium. Inward diffusion along grain boundaries may also be a possible source of retention, albeit somewhat small. It is the same low hydrogen solubility responsible for the generation of the open porosity that also prevents the large accumulation of implanted hydrogen isotopes in the beryllium. Tritium is simply unable to penetrate into the grains of the beryllium and decorate intrinsic and neutron produced traps. Unfortunately, as far as tritium inventory is concerned, tritium bred in the beryllium due to neutron induced nuclear reactions is unable to escape from the beryllium grains at low temperatures, leading to high tritium inventories in beryllium used for long periods of time in neutron producing fusion devices. Future studies on beryllium should concentrate on the use of single crystals to allow measurements of the true solubility and diffusivity.

Tungsten provides the tokamak operator with almost no short-term pumping of hydrogen isotopes. The recombination rate coefficient for hydrogen in tungsten is very high, and there may even be enhanced diffusion of the hydrogen in the implant zone when the implantation rate is high [61]. Still, high hydrdogen fluxes result in bubbles and eventually blisters. With or without the bubbles, the accumulation of 1.4 eV traps due to neutron irradiation will allow the hydrogen isotope inventory to slowly increase. Maintaining tungsten at an elevated temperature will likely alleviate both the blister and inventory problems. Future experimental work for tungsten should concentrate on high flux and fluence implantation. The effects of bubbles, blisters, trapping, and porosity on the hydrogen isotope retention needs further examination.

Carbon has the ability to provide the tokamak operator with temporary pumping. It is only necessary that helium glow discharge be used between shots to empty the near-surface saturated layer. As for tritium inventory, unless a way is found to conveniently remove hydrogen from the codeposited layer, the keyword for carbon is 'avoid'. Codeposition and trapping at neutron generated traps both provide for the potential accumulation of kilograms of hydrogen isotopes. When the isotope is tritium, this elevated inventory is not an acceptable choice. Future work should continue to be concentrated on removal of the codeposited layer and on the absorption and migration of hydrogen isotopes on pore surfaces.

Liquid metals appear to offer extremes in tritium retention and recycling. Lithium appears to be capable of offering elevated hydrogen isotope pumping during plasma exposure, lowering the recycling coefficient to almost zero. Tin and gallium, on the other hand, are not likely to pump hydrogen isotopes at all, providing 100% recycling. Research on the use of liquid metals in fusion reactor environments has just begun. Measurements of hydrogen diffusivity and recombination need to be determined for all liquid metal fusion reactor candidate materials.

Acknowledgements

This work was supported by the US Department of Energy under contract DE-AC04-94AL85000. The author would like to thank Ken Wilson for his encouragement, his suggestions, and his review.

References

[1] K.L. Wilson, R. Bastasz, R.A. Causey, et al., Nucl. Fus. 1 (1991) 31.
[2] K.L. Wilson, Nucl. Fus. (special issue), IAEA, Vienna, 1984 (Chapter 3).

[3] J. Ehrenberg, in: W.O. Hoffer, J. Roth (Eds.), Physical Processes of the Interaction of Fusion Plasmas with Solids: Plasma Materials Interaction Series, Academic Press, London, 1996.
[4] G. Gervansini, F. Reiter, Trans. Fus. Technol. 27 (1995) 30.
[5] T. Tanabe, N. Noda, H. Nakamura, J. Nucl. Mater. 196–198 (1992) 11.
[6] T. Tanabe, Suppl. J. Nucl. Fus. 5 (1994) 129.
[7] N. Yoshida, J. Nucl. Mater. 266–269 (1999) 197.
[8] G. Federici, R.A. Anderl, P. Andrew, et al., J. Nucl. Mater. 266–269 (1999) 14.
[9] P.G. Shewmon, Diffusion in Solids, McGraw-Hill, New York, 1963.
[10] A.S. Nowick, J.J. Burton, Diffusion in Solids, Recent Developments, Academic Press, New York, 1975.
[11] R.A. Swalin, Thermodynamics of Solids, Wiley, New York, 1972.
[12] M.A. Pick, K. Sonnenberg, J. Nucl. Mater. 131 (1985) 208.
[13] M.I. Baskes, J. Nucl. Mater. 92 (1980) 318.
[14] W.R. Wampler, Appl. Phys. Lett. 48 (6) (1986) 405.
[15] P.M.S. Jones, R. Gibson, J. Nucl. Mater. 21 (1967) 353.
[16] E. Abramov, M.P. Riehm, D.A. Thompson, J. Nucl. Mater. 175 (1990) 90.
[17] I.L. Tazhibaeva, V.P. Shestakov, E.V. Chikhray, et al., Proc. 18th Symp. Fus. Technol., 22–26 August, Karlsruhe, Fus. Technol. (1994) 427.
[18] D.A. Thompson, R.G. Macaulay-Newcombe, CFFTP Annual Report I-9425, 1994.
[19] D.A. Thompson, R.G. Macaulay-Newcombe, ITER Task T227 (1996), CFFTP Report G-9711, 1997.
[20] W.A. Swansiger, J. Vac. Sci. Technol. A 4 (3) (1986) 1216.
[21] V.I. Shapovalov, Y.M. Dukel'skii, Izv. Akad. Nauk SSSR Metally 5 (1988) 201.
[22] R.M. Al'tovakiy, A.A. Eremin, L.F. Eremina, et al., Russ. Metall. 3 (1981) 51.
[23] R.A. Anderl, M.R. Hankins, G.R. Longhurst, et al., J. Nucl. Mater. 196–198 (1992) 986.
[24] R.A. Causey, W.L. Hsu, B.E. Mills, et al., J. Nucl. Mater. 176&177 (1990) 654.
[25] R.A. Anderl, R.A. Causey, J.W. Davis, et al., J. Nucl. Mater. 273 (1999) 1.
[26] R.A. Langley, J. Nucl. Mater. 85&86 (1979) 1123.
[27] W.R. Wampler, J. Nucl. Mater. 122&123 (1984) 1598.
[28] W. Möller, B.M.U. Scherzer, J. Bohdansky, IPP-JET Report no. 26, 1985.
[29] W.R. Wampler, J. Nucl. Mater. 196–198 (1992) 981.
[30] A.A. Haasz, J.W. Davis, J. Nucl. Mater. 241–243 (1997) 1076.
[31] N. Yoshida, S. Mizusawa, R. Sakamoto, T. Muroga, J. Nucl. Mater. 233–237 (1996) 874.
[32] H.D. Falter, D. Ciric, J.P. Coad, D. Godden, JET Report R(97)03, 1997.
[33] R.G. Macaulay-Newcombe, D.A. Thompson, W.W. Smeltzer, Fus. Eng. Des. 18 (1991) 419.
[34] W.L. Hsu, R.A. Causey, B.E. Mills, et al., J. Nucl. Mater. 176&177 (1990) 218.
[35] R.A. Causey, G.R. Longhurst, W. Harbin, J. Nucl. Mater. 241–243 (1997) 1041.
[36] R.P. Doerner, A. Grossman, S. Luckhardt, R. Seraydarian, F.C. Sze, D.G. Whyte, J. Nucl. Mater. 257 (1998) 51.
[37] V.M. Sharapov, L.E. Gavrilov, V.S. Kulikauskas, A.V. Markin, J. Nucl. Mater. 233–237 (1996) 870.
[38] V.N. Chernikov, V.Kh. Alimov, A.V. Markin, et al., J. Nucl. Mater. 233–237 (1996) 860.
[39] V.Kh. Alimov, V.N. Chernikov, A.P. Zakharov, J. Nucl. Mater. 241–243 (1997) 1047.
[40] A.V. Markin, V.N. Chernikov, S.Y. Rybakov, A.P. Zakharov, J. Nucl. Mater. 233–237 (1996) 865.
[41] G. Saibene, R. Sartori, A. Tanga, et al., J. Nucl. Mater. 176&177 (1990) 618.
[42] R. Sartori, G. Saibene, H.H.J. Goodall, et al., J. Nucl. Mater. 176&177 (1990) 624.
[43] J. Ehrenherg, V. Phillips, L. De Kock, et al., J. Nucl. Mater. 176&177 (1990) 226.
[44] P. Andrew, M. Pick, J. Nucl. Mater. 220–222 (1994) 601.
[45] M. Mayer, J. Nucl. Mater. 240 (1997) 164.
[46] R.A. Causey, D.S. Walsh, J. Nucl. Mater. 254 (1998) 84.
[47] D.L. Baldwin, M.C. Billone, J. Nucl. Mater. 212–215 (1994) 948.
[48] D.V. Andreev, V.N. Bespalov, A.Ju. Birjukov, et al., J. Nucl. Mater. 233–237 (1996) 880.
[49] R. Sakamoto, T. Muroga, N. Yoshida, J. Nucl. Mater. 220–222 (1995) 819.
[50] R. Frauenfelder, J. Vac. Sci. Technol. 6 (3) (1969) 388.
[51] L.N. Ryabchikov, Ukr. Fiz. Zh. (Ukr. Phys. J.) 9 (1964) 293.
[52] A.P. Zakharov, V.M. Sharapov, E.I. Evko, Fiz. Khim. Mekh. Mater. 9 (2) (1973) 29.
[53] G. Benamati, E. Serra, C.H. Wu, J. Nucl. Mater. 283–287 (2000) 1033.
[54] C. Garcia-Rosales, P. Franzen, H. Plank, et al., J. Nucl. Mater. 233–237 (1996) 803.
[55] P. Franzen, C. Garcia-Rosales, H. Plank, V.Kh. Alimov, J. Nucl. Mater. 241–243 (1997) 1082.
[56] A. Mazayev et al., Izv. Akad. Nauk. USSR Metally 6 (1968) 233.
[57] E. Aitken et al., Trans. Met. Soc. AIME 239 (1967) 1565.
[58] R.A. Anderl et al., Fus. Technol. 21 (1992) 745.
[59] T. Nagasaki et al., J. Nucl. Mater. 202 (1993) 228.
[60] I. Takagi, H. fujita, K. Higashi, J. Nucl. Mater. 266–269 (1999) 697.
[61] R. Causey et al., J. Nucl. Mater. 266–269 (1999) 467.
[62] A.A. Haasz et al., J. Nucl. Mater. 258–263 (1998) 889.
[63] A. van Veen et al., J. Nucl. Mater. 155–157 (1988) 1113.
[64] H. Eleveld, A. van Veen, J. Nucl. Mater. 191–194 (1992) 433.
[65] H. Eleveld, A. van Veen, J. Nucl. Mater. 212–215 (1994) 1421.
[66] A. Pisarev, A. Varava, S. Zhdanov, J. Nucl. Mater. 220–222 (1995) 926.
[67] R.G. Macaulay-Newcombe, D.A. Thompson, J. Nucl. Mater. 263 (1998) 1109.
[68] V. Alimov, B. Scherzer, J. Nucl. Mater. 240 (1996) 75.
[69] V. Alimov, K. Ertl, J. Roth, J. Nucl. Mater. 290–293 (2001) 389.
[70] D.A. Komarov, A. Markin, S.Yu. Rybakov, et al., J. Nucl. Mater. 290 (2001) 433.
[71] R. Sakamoto, T. Muroga, N. Yoshida, J. Nucl. Mater. 233–237 (1996) 776.
[72] A. Haasz, M. Poon, J. Davis, J. Nucl. Mater. 266–269 (1999) 520.

[73] F. Sze, R. Doerner, S. Luckhardt, J. Nucl. Mater. 264 (1999) 89.
[74] T. Venhaus, R. Causey, R. Doerner, T. Abeln, J. Nucl. Mater. 290–293 (2001) 505.
[75] M.I. Guseva, V.I. Vasiliev, V.M. Gureev, et al., J. Nucl. Mater. 290–293 (2001) 1069.
[76] M. Mayer et al., J. Nucl. Mater. 230 (1996) 67.
[77] P. Tamm, L. Schmidt, J. Chem. Phys. 54 (1971) 4775.
[78] T. Venhaus, R. Causey, Fus. Technol. 39 (2001) 868.
[79] B.T. Kelly, Physics of Graphite, Applied Science, London, 1981.
[80] K.L. Wilson, W.L. Hsu, J. Nucl. Mater. 145–147 (1987) 121.
[81] W. Möller, J. Nucl. Mater. 162–164 (1989) 138.
[82] R.A. Causey, T.S. Elleman, K. Verghese, Carbon 17 (1979) 323.
[83] M. Saeki, J. Nucl. Mater. 131 (1985) 32.
[84] H.D. Rohrig, P.G. Fischer, R. Hecker, J. Am. Ceram. Soc. 59 (1979) 323.
[85] R.A. Langley, R.S. Blewer, J. Nucl. Mater. 76&77 (1978) 313.
[86] B.L. Doyle, W.R. Wampler, D.K. Brice, J. Nucl. Mater. 111&112 (1981) 513.
[87] K. Niwase, M. Sugimoto, T. Tanabe, F.E. Fujita, J. Nucl. Mater. 155–157 (1988) 303.
[88] R.B. Wright, R. Varma, D.M. Gruen, J. Nucl. Mater. 63 (1976) 415.
[89] Y. Gotoh, O. Okada, J. Nucl. Sci. Technol. 21 (1984) 205.
[90] Y. Gotoh, H. Shimizu, H. Murakami, J. Nucl. Mater. 162–164 (1989) 851.
[91] K. Ashida, K. Ichimura, M. Matsuyama, K. Watanabe, J. Nucl. Mater. 128&129 (1984) 792.
[92] D.K. Owens, H. Adler, P. Alling, C. Ancher, et al., J. Nucl. Mater. 220–222 (1995) 62.
[93] J.P. Biersack, L.G. Haggmark, Nucl. Instrum. and Meth. 174 (1980) 257.
[94] J. Winter, J. Vac. Sci. Technol. A 5 (1987) 2286.
[95] J. Winter, J. Nucl. Mater. 145–147 (1987) 131.
[96] E. Vietzke, V. Philipps, 3rd Workshop on Carbon Materials for Fusion Applications, Julich, 2 October 1987.
[97] E. Vietzke, K. Flaskamp, V. Phillipps, G. Esser, et al., J. Nucl. Mater. 145–147 (1987) 443.
[98] K. Besocke, G. Flentje, U. Littmark, H.G. Esser, et al., J. Nucl. Mater. 145–147 (1987) 651.
[99] W. Jacob, W. Möller, Appl. Phys. Lett. 63 (13) (1993) 1771.
[100] P. Reinke, W. Jacob, W. Möller, J. Appl. Phys. 74 (2) (1993) 1354.
[101] W. Jacob, Thin Solid Films 312 (1998) 1.
[102] J.P. Coad, B.G. Skorodumov, V.G. Ulanov, C.H. Wu, Vacuum 47 (6–8) (1996) 985.
[103] G. Federici, R. Anderl, J.N. Brooks, R. Causey, et al., Fus. Eng. Des. 39&40 (1998) 445.
[104] J. Winter, H.G. Esser, P. Wienhold, V. Phillipps, et al., Nucl. Instrum. and Meth. B 23 (1987) 538.
[105] R.A. Causey, W.R. Wampler, D. Walsh, J. Nucl. Mater. 176 & 177 (1990) 987.
[106] B. Dischler, A. Bubenzer, P. Koidl, Appl. Phys. Lett. 42 (1983) 636.
[107] A.R. Nyaiesh, W.B. Nowak, J. Vac. Sci. Technol. A 1 (1983) 308.
[108] J.C. Angus, J.E. Stultz, P.J. Shiller, J.R. MacDonald, et al., Thin solid Films 118 (1984) 311.
[109] M.P. Nadler, T.M. Donovan, A.K. Green, Appl. Surf. Sci. 18 (1984) 10.
[110] K. Maruyama, W. Jacob, J. Roth, J. Nucl. Mater. 264 (1999) 56.
[111] A.A. Haasz, S. Chiu, J.E. Pierre, Y.I. Gudimenko, J. Vac. Sci. Technol. A 14 (1) (1996) 184.
[112] J.W. Davis, A.A. Haasz, J. Nucl. Mater. 266–269 (1999) 478.
[113] W. Wang, V.Kh. Alimov, B.M.U. Scherzer, J. Roth, J. Nucl. Mater. 241–243 (1997) 1087.
[114] W.L. Hsu, J. Vac. Sci. Technol. A 7 (3) (1989) 1047.
[115] D.F. Cowgill, personal communication, submitted for publication.
[116] A. Refke, V. Phillips, E. Vietzke, J. Nucl. Mater. 250 (1997) 13.
[117] C.H. Skinner, H. Kugel, D. Mueller, B.L. Doyle, et al., J. Nucl. Mater. 241 (1997) 214.
[118] A.T. Peacock et al., J. Nucl. Mater. 266–269 (1999) 423.
[119] C.H. Skinner et al., Nucl. Fus. 39 (1999) 1081.
[120] A. von Keudell et al., Nucl. Fus. 39 (1999) 1451.
[121] W.N. Reynolds, Physical Properties of Graphite, Elsevier, Amsterdam, 1968.
[122] T. Kiyoshi, T. Namba, M. Yamawaki, J. Nucl. Mater. 155–157 (1988) 230.
[123] K. Flaskamp et al., Proceedings of the International Symposium on Plasma–Wall Interaction, Jülich, 1976, p. 285.
[124] R. Causey, M.I. Baskes, K.L. Wilson, J. Vac. Sci. Technol. A 4 (1986) 1189.
[125] R.A. Strehlow, J. Vac. Sci. Technol. A 4 (1986) 1183.
[126] B. Emmoth, M. Rubel, E. Franconi, Nucl. Fus. 30 (1990) 1140.
[127] R.E. Nightingale (Ed.), Nuclear Graphite, Academic Press, New York, 1962.
[128] R.M. Barrer, Proc. Royal Soc. (London) 149A (1935) 253.
[129] W.J. Thomas, J. Chim. Phys. 57 (1960) 61.
[130] R.C. Bansal, F.J. Vastola, P.L. Walker, Carbon 9 (1971) 185.
[131] A.J. Robell, E.V. Ballou, M. Boudart, J. Phys. Chem. 68 (1964) 2748.
[132] D.R. Olander, M. Balooch, J. Catal. 60 (1979) 41.
[133] R.D. Penzhorn, N. Befris, U. Berndt, et al., J. Nucl. Mater. 288 (2001) 170.
[134] V. Malka, H.D. Rohrig, R. Hecker, Proceeding Conference on Tritium Technology in Fission, Fusion, and Isotope Applications, 1980, p. 102.
[135] H. Atsumi, S. Tokura, M. Miyake, J. Nucl. Mater. 155–157 (1988) 241.
[136] R.A. Causey, J. Nucl. Mater. 162–164 (1989) 151.
[137] H. Atsumi, M. Iseki, T. Shikama, J. Nucl. Mater. 191–194 (1992) 368.
[138] H. Atsumi, M. Iseki, T. Shikama, J. Nucl. Mater. 212–215 (1994) 1478.
[139] W.R. Wampler, B.L. Doyle, R.A. Causey, K. Wilson, J. Nucl. Mater. 176&177 (1990) 983.
[140] R.A. Causey, K.L. Wilson, W.R. Wampler, B.L. Doyle, Fus. Technol. 19 (1991) 1585.
[141] R.A. Causey, W. Harbin, D. Taylor, L. Snead, Phys. Scrip. T 64 (1996) 32.

[142] S.L. Kanashenko, A.E. Gorodetsky, V.N. Chernikov, A.V. Markin, et al., J. Nucl. Mater. 233–237 (1996) 1207.
[143] V.Kh. Alimov, R. Schworer, B.M.U. Scherzer, J. Roth, J. Nucl. Mater. 187 (1992) 191.
[144] A.A. Haasz, J.W. Davis, J. Nucl. Mater. 232 (1996) 219.
[145] M. Mayer, M. Balder, R. Behrisch, J. Nucl. Mater. 252 (1998) 55.
[146] R. Causey, W.R. Wampler, O.I. Buzhinshij, J. Nucl. Mater. 196–198 (1992) 977.
[147] Y. Hirooka, R. Conn, R. Causey, G. Chevalier, et al., J. Nucl. Mater. 176&177 (1990) 473.
[148] H. Moriyama, K. Iwasaki, Y. Ito, J. Nucl. Mater. 191–194 (1992) 190.
[149] E.E. Shpil'rain et al., High Temp. 3 (1965) 870.
[150] R.E. Buxbaum, E.F. Johnson, Ind. Eng. Chem. Fundam. 24 (1985) 180.
[151] R.M. Alire, J. Chem. Phys. 65 (1976) 1134.
[152] G.R. Longhurst et al., TMAP user's manual, EFF-FSP 10315, Idaho National Engineering and Environmental Laboratory, 12 June 1992.
[153] E.L. Cussler, Multicomponent Diffusion, Elsevier, New York, 1976 (p. 308).
[154] M. Hoch, J. Nucl. Mater. 120 (9184) 102.
[155] H. Katsuta, T. Ishigai, K. Furukawa, Nucl. Technol. 32 (1977) 297.
[156] E. Veleckis et al., J. Phys. Chem. 78 (1974) 1933.
[157] K. Iwase, Sci. Rep. Tohoku Univ., First Ser. 15 (1926) 531.
[158] W.M. Mueller, J.P. Blackledge, G.G. Libowitz, Metal Hydrides, Academic Press, New York, 1968, p. 573.
[159] S.K. Erents, G.M. McCracken, P. Goldsmith, J. Phys. D (1971) 672.
[160] M.J. Baldwin, R.P. Doerner, et al., J. Nucl. Mater. 290–293 (2001) 166.